Analysis of the work-to-heat conversion beyond the necking onset in non-isothermal tensile tests

International Journal of Impact Engineering 207 (2026) 105503

Contents lists available at ScienceDirect

International Journal of Impact Engineering

journal homepage: www.elsevier.com/locate/ijimpeng

# Analysis of the work-to-heat conversion beyond the necking onset in non-isothermal tensile tests

Marta Beltramo *, Martina Scapin, Lorenzo Peroni

*Department of Mechanical and Aerospace Engineering, Politecnico di Torino, Turin, Italy*

ARTICLE INFO

*Keywords:*
Self-heating
Necking
Specimen deformed shape
Infrared imaging
Taylor-Quinney coefficient
Thermo-mechanical response

ABSTRACT

When metals undergo plastic deformation at sufficiently high speed, the plastic work dissipated as heat can cause material self-heating, influencing the material's mechanical behavior. This phenomenon is particularly critical during localized deformation. The present study proposes two methods for investigating the work-to-heat conversion during the post-necking phase of tensile tests on cylindrical dog-bone samples. One method directly applies the heat equation and is developed for adiabatic conditions only; the other method requires iterative thermal-structural finite element simulations but is also applicable to non-adiabatic conditions. Both methods involve recording the tests with optical and infrared cameras with adequate temporal and spatial resolution to fully exploit the heterogeneous fields and to improve the reliability of the results. A key distinction from other studies is the avoidance of using Digital Image Correlation technique, opting instead for a method based on necking silhouettes, which reduces experimental complexity and avoids issues related to speckle damage. Both the direct and iterative approaches, after being successfully tested against numerical benchmarks, were applied to an experimental case study. The material tested was 17–4PH martensitic stainless steel, known for its moderate strain rate sensitivity and substantial self-heating due to low thermal conductivity. Tests were conducted at room temperature and at nominal strain rates of 1, 10, and 1000 $s^{-1}$. The results demonstrated the practical applicability of the proposed methods, suggesting their potential for investigating the work-to-heat conversion up to large strains by exploiting the post-necking phase of tensile tests with limited experimental complexity.

## 1. Introduction

When metals deform plastically, part of the plastic work is stored in the material as defects, while the rest (usually the majority) is dissipated as heat. If the deformation process is fast enough, temperature increases occur in the material because the heat generated by plastic deformation cannot be fully exchanged with the surrounding environment. This resulting temperature increase can affect the material's mechanical response, a phenomenon typically referred to as thermal softening.

To accurately predict temperature fields and the consequent mechanical response, it is essential to properly account for heat generation caused by plastic deformation. This is important for optimizing material performance in various fields, such as metal forming, high-speed machining, etc. Generally, the issue of rising temperature due to plastic deformation is of practical interest whenever phenomena like fast plastic deformation, shear banding, dynamic void growth, and dynamic fracture are involved. Hence, it is worth investigating the coupling between plastic deformation and heat generation. A comprehensive review of this topic was recently presented by Nassar [1].

In thermos-mechanics, the fraction of plastic work converted into heat is usually referred to as the Taylor-Quinney Coefficient $\beta$ (TQC), named after the researchers who first conducted experiments to investigate this issue [2]. In coupled thermo-mechanical problems, the thermal field $T$ and the mechanical field are linked through the heat conduction equation [3]:

$$\dot{T} = \alpha \nabla^2 T + \frac{\beta}{\rho c_p} \dot{W}_p - \frac{k}{\rho c_p} \frac{E}{1-2\nu} T_0 tr(\dot{\varepsilon}_e), \tag{1}$$

where $\alpha$ is the thermal diffusivity, $\rho$ is the density, $c_p$ is the specific heat, $\dot{W}_p$ is the rate of plastic work, $k$ is the coefficient of thermal expansion, $E$ is the Young's modulus, $\nu$ is the Poisson's ratio, $T_0$ is the initial temperature, and $\dot{\varepsilon}_e$ is the elastic strain rate tensor. The left term represents the change in internal energy, which depends on heat conduction (the first term on the right), irreversible plastic deformation (the second term on the right [2,4]), and reversible thermoelastic effect (the third term on

* Corresponding author.
*E-mail address:* marta.beltramo@polito.it (M. Beltramo).

https://doi.org/10.1016/j.ijimpeng.2025.105503
Received 20 April 2025; Received in revised form 10 July 2025; Accepted 10 August 2025
Available online 11 August 2025

the right). This last term is usually negligible when large plastic deformation occurs, leading to the simplified equation:

$$\dot{T} = \alpha \nabla^2 T + \frac{\beta}{\rho c_p} \dot{W}_p. \tag{2}$$

When the deformation speed is such that adiabatic conditions can be assumed, Eq. (2) simplifies further by taking advantage of the fact that no heat conduction occurs [3,5–13]. In these cases, it results:

$$\beta = \frac{\rho c_p \dot{T}}{\dot{W}_p}. \tag{3}$$

Over the past decades, significant efforts have been devoted to studying work-to-heat conversion using both physical and phenomenological approaches. Physical models have focused on the underlying mechanisms responsible for energy storage in metals: for example, models were developed based on residual stress [14] or dislocation theories [15]. To bridge theory and experiments, the stored energy of cold work has also been quantified within thermodynamically consistent frameworks, as shown by Rosakis et al. [16] and Lieou and Bronkhorst [17]. In parallel, advanced numerical methods, such as crystal plasticity [18], dislocation dynamics [19], and molecular dynamics [20] have increasingly contributed to uncovering the energy storage physics. At the same time, phenomenological approaches continue to receive considerable attention. While these models may lack a direct physical interpretation, their strength lies in not requiring detailed knowledge of microscopic mechanisms, which can be complex and difficult to capture theoretically. This makes them particularly attractive for industrial applications, as they offer experimentally informed TQC. As a result, research on empirical methods remains active, with ongoing efforts to improve their accuracy and applicability. The present work falls within this category, and the following paragraphs focus on empirical strategies to establish the context of this study.

Empirical approaches generally employed experimental measurements to directly apply Eq. (3) in case adiabatic conditions are satisfied. More specifically, to apply this equation, it is necessary to measure the temperature and plastic work and compute their time derivatives. In some cases, another quantity is used to obtain an engineering measure of thermomechanical conversion efficiency. This is denoted as $\beta_{int}$ and is defined as:

$$\beta_{int} = \frac{\rho c_p \Delta T}{W_p}, \tag{4}$$

where $W_p$ and $\Delta T$ represent the total plastic work and total temperature increment up to a given moment of the test. For clarity and consistency with past research, the TQC in Eq. (3) will be referred to as $\beta_{diff}$.

The distinction between the two definitions was first pointed out by Rittel, 1999 [21]: $\beta_{diff}$ refers to the power ratio (thus describing the rate of energy conversion at a specific configuration), while $\beta_{int}$ refers to the energy ratio (describing the total converted energy up to a certain configuration). For constitutive description of materials, $\beta_{diff}$ must be considered since it better reflects how the partition of plastic work evolves during deformation. The main drawback is that experimental evaluation of $\beta_{diff}$ is more prone to noise and less stable than $\beta_{int}$. Hence, $\beta_{int}$ has been widely used in literature, especially in conjunction with experimental analysis [7,8,11,12,22].

Regardless of the definition chosen, experimental approaches that directly apply Eqs. (3) or (4) require the evaluation of plastic work. Thus, strain and stress measurements are necessary; then such data are combined with temperature measurements to estimate the TQC. Traditionally, when high strain rate tests were performed with a Hopkinson or Kolsky bar apparatus, the theory of one-dimensional wave propagation was used to determine strain, strain rate and stress during tests [3,5–8,10–12].

For temperature measurements during high strain rate tests, infrared detectors have been widely used due to their short response time and fast acquisition rate [3,5–8]. In recent years, infrared imaging has been increasingly employed, allowing for full-field measurements. Under the assumption of uniform and adiabatic deformation, full-field thermal data are used to enhance measurement stability by averaging the temperature over a region of the sample [9–11]. For example, Vazquez-Fernandez et al. [9] used infrared images to qualitatively assess whether adiabatic behavior was a reasonable assumption. Indeed, during uniform deformation, adiabatic conditions are expected to generate a homogeneous temperature field in the gauge section; if this does not occur, the assumption of adiabaticity is incorrect. As shown in a comparison study by Goviazin et al. [23], the main limitation of using high-speed cameras, compared to infrared detectors, under dynamic loading conditions, is the lower sampling rate. Conversely, high-speed cameras are especially suitable for measuring local deformation.

Hence, infrared imaging is most effective when used for full-field measurements of heterogeneous temperature fields generated by non-adiabatic conditions and/or complex stress states. For example, they were used to observe dissipative effects due to strain localization and Lüders band propagation [24–27] or to Portevin-Le Chatelier effect [28,29]. Generally, when dealing with heterogeneous thermal fields in the context of work-to-heat conversion, infrared images are often combined with the Digital Image Correlation (DIC) technique for full-field strain measurements. A detailed review on this topic can be found in Soares et al. [30]. In these applications, associating the kinematic data of a material point to thermal measurements of the same point (in a Lagrangian approach) is quite challenging. Methods were developed for low strain rate tests: a motion compensation technique was applied to thermal data by Pottier et al. [31]; an Eulerian approach was adopted by Knysh and Korkolis [32] (by focusing on a single point fixed in space); algorithms to map the deformation field from DIC analysis on the temperature field were employed by Nowak and Maj [33]. Conversely, to avoid using such complex approaches, Dæhli et al., in their study on non-adiabatic tensile tests on notched sheet specimens [34], proposed limiting the analysis to the maximum temperature within a predefined subdomain that always includes the central region of the sample. In addition to all the above aspects related to data acquisition and post-processing, when investigating the work-to-heat conversion, it is necessary to account for all heat transfers. This implies that at medium-low strain rates heat loss phenomena, primarily conduction and convection, must be considered. In the quasi-static tensile tests analyzed by Knysh and Korkolis [32], Eq. (1) (in its Eulerian form) was directly used to estimate the TQC from DIC and infrared thermography measurements. This was possible because the specimen was subjected to a uniaxial stress state (due to its slenderness and because the tests were considered only until the necking onset). In other cases, such as quasi-static tensile tests on notched samples, this simplification could not be adopted, and inverse methods were used. Parameters of a finite element (FE) model were iteratively adjusted until satisfactory results were achieved. Typically, given the limited temperature rise in quasi-static tests, the plastic and thermal responses could be uncoupled. Thus, a first optimization determined the constitutive behavior by looking at the force vs. elongation curve, and then a second optimization identified the TQC by comparing temperatures [31,34].

Overall, an interesting field of application for infrared imaging in material testing is in test conditions where the specimen exhibits a heterogeneous thermal field. This is also the case of tensile tests beyond the necking onset [13,30,35–37]. Indeed, as anticipated, temperature increases (and the consequent thermal softening) are of primary importance when localized deformation occurs. This also means that tests where localized deformation occurs can provide information about the dissipation of plastic work into heat at large strains. In the context of work-to-heat conversion, several studies focused on tensile tests, thanks to their ease of execution and the possibility of carrying out tests at different strain rates and/or initial temperatures. However, most of these analyses were limited to the pre-necking phase [7,9,12].

Nevertheless, with the onset of necking in ductile metals, tensile tests can be further exploited by also using data collected during necking. For instance, Smith et al. [13] computed the TQC at different locations along the length of a flat specimen by exploiting full-field deformation and temperature measurements. This allowed them to gather information about the heat conversion at strains higher than that at the necking onset, provided that adiabatic conditions were verified.

The present study contributes to this field by introducing innovative solutions for analyzing work-to-heat conversion during the post-necking phase of both adiabatic and non-adiabatic tests. Specifically, tensile tests on axisymmetric dog-bone samples made of isotropic metals are considered, and two methods are presented: one applicable only to adiabatic conditions and another one applicable even to non-adiabatic conditions. Like other existing strategies, the method entails recording the test with both visible and infrared cameras with adequate temporal and spatial resolution. However, a key difference from other studies is that, instead of the DIC technique, an alternative method is employed that exploits the axial symmetry of the necking shape of isotropic materials to reduce the experimental effort. In particular, only the necking silhouette is considered, through a procedure previously developed by the authors [38]. Since this method consists of searching for the experimental specimen's shapes within a database built from FE simulations, the equivalent plastic strain on the specimen's surface is obtained with limited experimental and computational effort and without assuming uniform strain on the cross-sections. This strategy pursued the aim of developing efficient empirical methods, from both the experimental and analysis perspectives, for investigating the TQC up to large strains. Moreover, a wide axial portion around the profile center was considered in the analysis, allowing for full exploitation of the heterogeneous thermal and mechanical data, leading to more reliable results.

To better understand the proposed methods, Section 2 provides background information on the method presented by the authors in [38]. This approach, referred to as the "Database approach", forms the basis for the methods proposed in the present paper. The proposed methods are then presented and thoroughly described in Section 3, along with numerical examples. Finally, an experimental case study is presented in Section 4: the experimental setup is described along with additional considerations on temperature measurement, followed by the presentation and critical analysis of the results.

## 2. Overview of the database approach

To ensure a clear understanding of the present work, the basic principles of the database approach are outlined below, with the aid of the workflow shown in Fig. 1 (for further details, see [38]).

The core idea is to rely on a database that collects the results of FE simulations of tensile tests on cylindrical samples exhibiting isotropic Von Mises plasticity and different hardening behaviors. This database establishes a relationship between the specimen's external contour during necking and the superficial distributions of equivalent plastic strain, strain rate and equivalent stress associated with that specific necking shape.

Since the proposed approach is based on the specimen's necking profile, acquiring high-quality images with clear contrast between the sample and the background is essential. For this reason, backlighting is recommended. The acquired images are post-processed using edge detection algorithms to determine the specimen's external contours. Exploiting material isotropy and the axisymmetric geometry of the sample (which are the hypothesis at the basis of the database approach), average semi-profiles are then derived.

For each necking semi-profile (i.e., for each time) an algorithm searches the database for the numerical shape that most closely matches the experimental one. To limit the size of the database, the comparison between experimental and numerical profiles is performed in terms of relative shape. Thus, the best numerical profile is the one that is overlapped with the experimental shape after optimal scaling (using the same factor for both radial and axial coordinates). This database profile comes from a tensile test simulated on a "virtual" material with a specific hardening law. This law accurately represents the behavior of the real material in a neighborhood of the time considered. Therefore, the spatial distributions of strain, strain rate, and stress in the experimental profile at that moment are reasonably approximated by those of the numerical profile (after proper processing due to the database reduction technique). Practically, from the simulation that generated that numerical

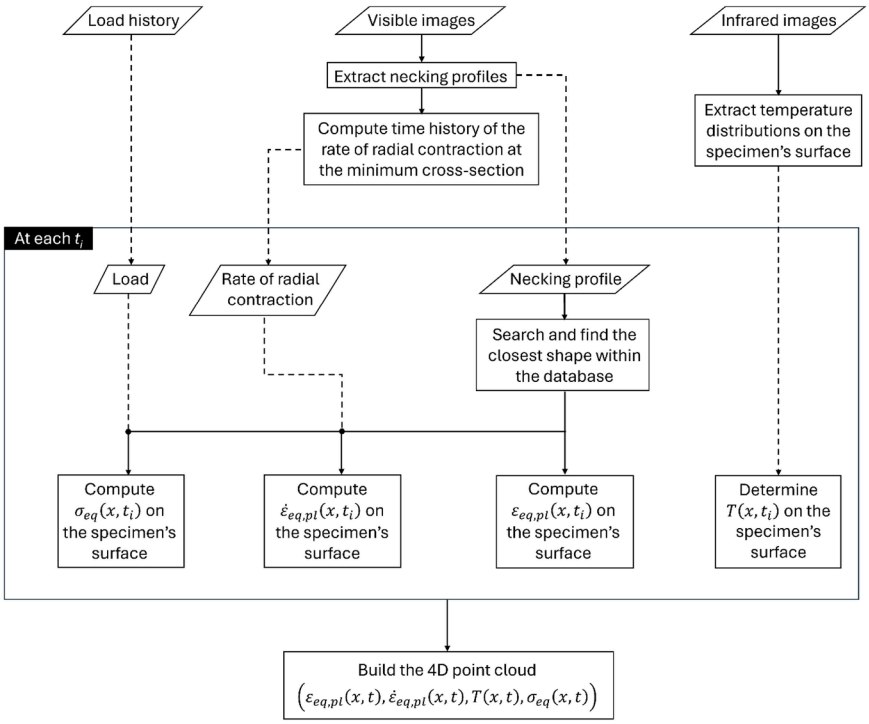


**Fig. 1.** Schematic representation of the determination of Eulerian fields with the database approach.

profile, all local values of strain, strain rate and stress at that configuration are considered. Then, the distributions of equivalent plastic strain, strain rate and equivalent stress on the real specimen's surface can be determined by properly considering the test speed and the force at that instant.

These distributions can be combined with experimental temperature measurements obtained by an infrared camera at the same time. The result is the set of fields $\varepsilon_{eq,pl}(x)$, $\dot{\varepsilon}_{eq,pl}(x)$, $\sigma_{eq}(x)$, and $T(x)$ at the given time, where $x$ is the axial coordinate of points on the specimen's surface. By applying this method at multiple times, the temporal evolution of these fields is determined, leading to the construction of a 4D point cloud $\left(\varepsilon_{eq,pl}, \dot{\varepsilon}_{eq,pl}, T, \sigma_{eq}\right)$ that represents the material response during the test. Since both infrared and optical cameras observe a fixed region in space, the description provided by the database approach is Eulerian.

To conclude, it is worth emphasizing that the database approach in the form presented in this work is applicable only to round specimens made of isotropic materials. Nevertheless, within this scope, it offers an experimentally simpler alternative to the DIC technique, still effectively capturing the heterogeneous strain fields characteristic of necking. Moreover, it provides a means to estimate the instantaneous strain rate and equivalent stress experienced by material points on the specimen's surface, without requiring any simplifying assumption. The results obtained through the database approach are used by both methods proposed in this paper for TQC estimation, albeit in different ways. A detailed explanation of how this data is used by each method is provided in the next section.

## 3. Proposed methods

As anticipated, this study proposes two methods for analyzing the work-to-heat conversion during the post-necking phase of tensile tests. A schematic representation of the proposed approaches is depicted in Fig. 2.

Both methods involve monitoring the applied load during the tests and imaging the specimens with optical and infrared cameras. The initial stage of data analysis is common to both approaches and consists of applying the database approach, as anticipated in Section 2. Then, the two approaches diverge, and their specific procedures are detailed in the following sections. One method was developed for adiabatic conditions only and will be referred to as "Direct approach". The other method is a preliminary approach that can be applied even under non-adiabatic conditions. Since this method requires some iterations to converge, it will be called "Iterative approach". Although the iterative approach is more general, it is still worth exploring the direct approach because of its higher efficiency (when applicable, i.e., under adiabatic conditions). Sections 3.1 and 3.2 focus on the direct and iterative approach respectively.

### 3.1. Direct approach

As the name suggests, this method aims to estimate the TQC by directly applying Eqs. (4) (or (3)) to different material points. This requires determining, for each material point, the temperature history together with the strain and stress histories (which are necessary for computing the plastic work). Temperature is provided by infrared images, while strain and stress data are obtained from proper analysis of load history and optical images using the database approach. The key difference of the proposed direct method, compared to other direct methods in the literature, mainly lies in its strategy for simultaneous strain and stress analysis, offering an alternative for round specimens of isotropic materials to the combined use of DIC and plastic flow identification techniques.

As anticipated, the database approach provides an Eulerian description of the deformation process, but to directly study the conversion of work into heat, a Lagrangian perspective would be more convenient. Even in the simple case of adiabatic conditions and negligible thermoelastic effect, the Eulerian form of Eq. (1) would require computing the velocity field and temperature gradient. Due to the difficulty and uncertainty in calculating these quantities, the Lagrangian approach was preferred.

This approach entails tracking material points; however, backlighting – which is recommended to acquire high-contrast images – prevents direct tracking of material points (except for the profile center). Despite this, the ability to track different material points enables full use of the thermal data obtained from infrared imaging. This enhances the stability and reliability of the results when studying work-to-heat conversion, compared to considering only the point at the superficial necking center. To address this, a suitable technique has been developed and is described in Section 3.1.1. This method allows the imaging setup to be optimized for edge detection (with backlighting) while maintaining the capability to track points during necking.

Thanks to this tracking technique, it is possible to convert the Eulerian fields of strain, stress and temperature into the corresponding Lagrangian fields. In other words, the time evolution of strain, stress and temperature of different material points is obtained. Then, it is possible to compute the plastic work done on each material point by integrating its deformation path in the plane $\varepsilon_{eq,pl} - \sigma_{eq}$. Finally, according to Eq. (4), the ratio between the temperature increase and the plastic work represents the evolution of the integral TQC at different material points. Similarly, Eq. (3) can be used to evaluate the differential TQC. An example based on a numerical benchmark is presented in Section 3.1.2.

This direct approach also facilitates the investigation of correlations between TQC and variables like strain, strain rate and temperature (even within a single test). Indeed, past research has provided evidence of the dependence of work-to-heat conversion on various factors, such as the strain (e.g., in [5,9,10,12,21,34,37]) and the strain rate (e.g., in [5,9,12,21,39]). The advantage of direct methods, when applicable, lies in their ability to study these dependencies as "a posteriori" evaluations, without relying on preconceived assumptions.

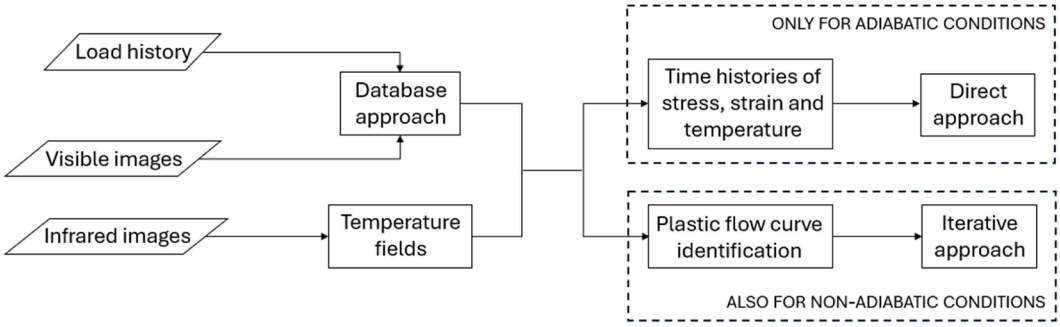


**Fig. 2.** Schematic representation of the proposed methods for investigating the work-to-heat conversion.

### 3.1.1. Tracking strategy

The tracking strategy proposed in this paper combines the 1D necking model by Audoly and Hutchinson [40,41] with the database approach [38].

Audoly and Hutchinson's theory is an analytical framework that kinematically describes the evolution of necking using a Lagrangian description of the deformation. It establishes a relationship between the initial positions of material points and their positions in a deformed configuration. Initially developed for strain rate insensitive materials [40], this theory was later extended to strain rate sensitive materials [41]. The present authors have previously applied this theory [42] to determine the deformed axial positions of material points given their initial axial positions on the specimen surface. In this study, the theory is not used in that sense because the database, being built from numerical simulations, already contains the correlation between the initial and deformed positions of material points. Instead, the 1D theory is used as the theoretical foundation of the approach. Indeed, the 1D theory proves that the kinematics of necking are independent of the material. While the material determines the resulting shape, it does not affect how the deformed positions of the material points are related to their initial positions. This relationship is solely dependent on the shape itself.

To summarize, the above-mentioned 1D theory justifies the material independence of the correlation between undeformed and deformed configurations. However, it is the database that specifically provides this relationship for the available shapes. Hence, if the experimental necking shape is well-approximated by a numerical one, the same correlation between undeformed and deformed configuration applies.

As noted in Section 2, the technique used to limit the size of the database requires proper processing of the results extracted from the database. This is necessary also for the relationship between deformed and undeformed positions. The best numerical shape provides the desired correlation $x(X)$ but the geometrical scaling of the shape must be considered. In other words, it is necessary to understand which material points of the numerical sample best represent real material points. To determine the proper post-processing technique, the 1D theory was employed, as explained in Appendix A. Only the final results are presented here, with the aid of Fig. 3; uppercase letters represent the initial positions of material points, while lowercase letters denote the corresponding deformed position at a certain necking configuration.

First, consider that the best numerical shape (denoted as "DB") should be scaled down by a coefficient $k_g$ to overlap with the experimental specimen shape ("SP deformed"). Referring to Fig. 3a, the numerical shape "DB scaled" overlaps with the experimental one. Analogous points are those that overlap after scaling (dots and vertical lines in Fig. 3a both in the undeformed and deformed configurations). For example, in Fig. 3a, the points $(x_{SPi}, r_{SPi})$ and $(x_{DBi}, r_{DBi})$ are analogous, being $x_{DBi} = x_{SPi}k_g$ and $r_{DBi} = r_{SPi}k_g$. Since each point is identified by its position in the undeformed configuration ($X_{SPi}$ and $X_{DBi}$ for the example of Fig. 3a), determining which material points of the numerical sample best represent real material points requires establishing the relationship between the initial positions of analogous points (e.g., $X_{SPi}$ and $X_{DBi}$).

From the 1D theory, it can be proved that $X_{DBi} = k_g^3 X_{SPi}$ in case the initial radius of both the real specimen and the virtual one are the same (see Appendix A). Therefore, once a set of points $X_{SP}$ on the specimen's surface is chosen, their deformed positions coincide with the deformed positions of points in the FE model with initial position $X_{DB} = k_g^3 X_{SP}$. Next, since the correlation between $X_{DB}$ and $x_{DB}$ is known from the simulation, it can be interpolated to determine the deformed position $x_{SP}$ of the material points that initially were at $X_{SP}$ (as shown in Fig. 3b). By repeating this procedure at different times during necking (i.e., on different necking shapes), it becomes possible to track material points throughout the deformation.

A potential concern with this tracking technique could be its application to dog-bone specimens made of strain rate sensitive materials. The theoretical framework was developed for slender cylinders, and the database was built from virtual tensile tests on slender cylinders made of strain rate insensitive materials. To address this, numerical investigations were conducted to verify the reliability of the newly proposed tracking technique. Some numerical benchmarks are shown in the next section.

### 3.1.2. Numerical examples

In this section, the application of the proposed direct approach is shown through ad-hoc numerical benchmarks.

Monotonic tensile tests were simulated using the commercial FE code Ansys LS-DYNA. The sample geometry was a cylindrical dog-bone specimen with a gauge length of 5 mm and a gauge radius of 3 mm (matching the geometry used by the authors in the experimental application presented in Section 4). Axisymmetric shell elements with one integration point were used to model one quarter of the specimen. A symmetry boundary condition was applied at the midline of the gauge length, while a prescribed displacement was imposed at the specimen head. For the material model, the virtual tests analyzed here employed the Johnson-Cook model of Armco Iron with the parameters reported by Johnson and Cook [43]:

$$\sigma_{eq} = \left(175 + 380\varepsilon_{eq,pl}^{0.32}\right)\left(1 + 0.06\ln\left(\dot{\varepsilon}_{eq,pl}\right)\right)\left(1 - \left(\frac{T-298}{1811-298}\right)^{0.55}\right). \text{ (MPa)} \tag{5}$$

The density and heat capacity were considered constant and equal to 7890 kg/m$^3$ and 452 J/(kg·K) respectively (taken from [43] too). Due to its significant strain rate and temperature sensitivity, this material serves as a relevant case study. Adiabatic conditions were considered, consistent with the underlying hypothesis of the direct approach. As anticipated, past research provided evidence of the dependence of work-to-heat conversion on various factors. In this study, the authors focused on two cases: constant TQC and strain-dependent TQC. This was implemented in Ansys LS-DYNA using a material model in which the

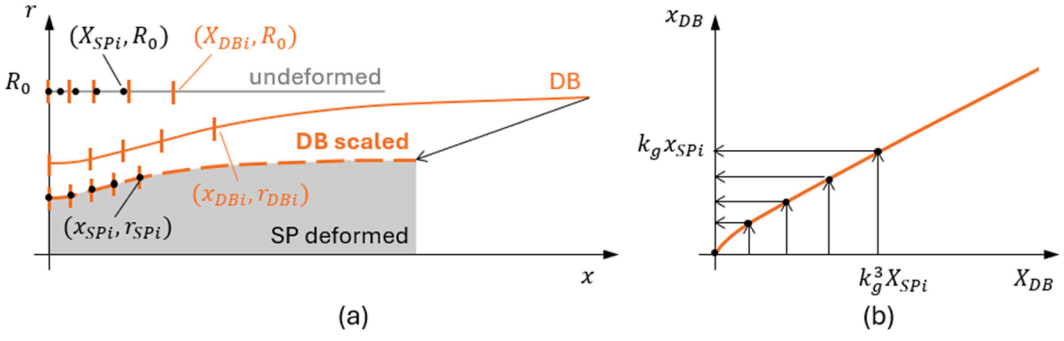


**Fig. 3.** Technique for tracking material points with the database approach. a) Comparison of the shapes and representation of analogous material points. b) Correlation between deformed and undeformed axial positions of superficial material points for the database.

TQC can depend on different variables and in which the effect of strain rate and temperature on the flow stress are uncoupled and tabularly defined (*MAT_224).

For each simulated test, several necking configurations were selected, and for each of them the closest matching shape in the database was identified, along with the corresponding scaling coefficient $k_g$. This best numerical shape established the correlation $x(X)$ between undeformed and deformed positions of material points for that configuration.

Simultaneously, for each benchmark case, the material points to be tracked were chosen to coincide with FE nodes. Their initial axial positions in the undeformed configuration are denoted $X_{SP}$. As explained in Section 3.1.1, the equivalent points in the database are those initially located at $X^*_{DB} = k_g^3 X_{SP}$. Hence, by interpolating the function $x(X)$ at $X^*_{DB}$, the deformed positions $x_{SP}$ of the selected material points were determined. Since these points also correspond to FE nodes in benchmark simulations, it was possible to directly compare the predictions from the database with the FE simulation itself. An example of this comparison, for the case of variable TQC, is shown in Fig. 4.

Both cases of constant and of variable TQC were found to give a tracking error of approximately 0.3 % when considering the entire gauge length. This error was calculated as average relative error on the axial position of $N_n$ nodes in the gauge length for $N_{cfg}$ different configurations:

$$error = \frac{1}{N_{cfg}} \sum_{i=1}^{N_{cfg}} \left[ \frac{1}{N_n} \sum_{j=1}^{N_n} \left( \frac{x_{ij} - \widetilde{x}_{ij}}{x_{ij}} \right) \right], \tag{6}$$

where $x_{ij}$ is the reference value from the FE simulation, and $\widetilde{x}_{ij}$ is the value estimated with the proposed tracking technique.

From Fig. 4 it can be noticed that points located farther from the neck are subjected to boundary effects. The table included in Fig. 4 also shows that the tracking error decreases when the considered portion of the initial gauge length is reduced ($X_{max}$ is the maximum distance from the sample's center). This trend is reasonable, given that the database was built using cylindrical specimens, whereas the benchmark simulations were performed on dog-bone samples.

Overall, the proposed tracking strategy was demonstrated to be accurate, especially considering that regions far from the neck (that are affected by a higher error) will not be considered in analyzing the work-to-heat conversion, as will be discussed in the next paragraph.

As stated in Section 2, once the closest shape in the database was identified, the surface distributions of equivalent plastic strain and equivalent stress could also be retrieved. By combining this information with the tracking of material points, the time evolutions of $\varepsilon_{eq,pl}$ and $\sigma_{eq}$ were found for each tracked point. This converts the Eulerian fields provided by the database approach into Lagrangian fields. Since these are numerical benchmarks, the equivalent plastic strain and equivalent stress obtained from the database could be directly compared to the corresponding values from the FE simulations. Results are shown only for the variable TQC case, as the constant TQC case produced similar outcomes. Fig. 5 presents the percentage errors along the specimen surface at various configurations (the same reported in Fig. 4). Each profile was normalized by its radius at the minimum cross-section to enhance the readability of the plots. A Lagrangian perspective was adopted, with the abscissa being the initial axial position of material points. Theoretically, this representation is influenced by both the tracking accuracy and the estimation of Eulerian fields. However, since tracking errors were shown to be very small (see Fig. 4), these plots primarily reflect the accuracy of the estimated strain and stress fields.

The results indicate that a good prediction of both strain and stress was achieved across a substantial portion of the profile. Nevertheless, the error increases towards the extremities of the gauge length. This may be attributed to the previously mentioned geometric effect (cylindrical vs. dog-bone sample). Moreover, it should also be considered that during necking progressive unloading occurs, hence the parts affected by a higher error are also those that are no longer in the plastic domain, and therefore that do not give additional information on the plastic work. Thus, they were withdrawn from the subsequent analysis, without influencing the effectiveness of the proposed method.

It is worth underlining that, although adiabaticity was considered in these tests, such hypothesis was not necessary for the analyses conducted up to now. Both the tracking strategy and the analysis of stress and strain fields remain valid regardless of whether adiabatic conditions are met.

Adiabaticity assumption becomes essential when computing the work-to-heat conversion using the direct approach. For this purpose, the time history of temperature at different material points was required too. It suffices to interpolate the thermal spatial distributions onto the points identified through the tracking strategy. These results are affected by the tracking error, but, as previously shown, this error has only a minor impact. The time evolution of plastic work and temperature increase for various material points were then used to compute the integral TQC using Eq. (4). The resulting point cloud is shown in Fig. 6a for both the cases of constant and variable TQC. For determining the differential TQC, time differentiation was necessary. To reduce the noise, one possibility is to fit the plastic work and temperature increment histories and then apply Eq. (3) (as done by Smith et al. [12]). In contrast, this paper adopts an alternative approach to compute the differential TQC: the point cloud of integral TQC values was fitted with a mathematical function, to which the following expression (derived in Appendix B) was applied:

$$\beta_{diff}(\varepsilon) = \frac{d\beta_{int}}{d\varepsilon}\varepsilon + \beta_{int}. \tag{7}$$

The resulting $\beta_{diff}(\varepsilon)$ are presented in Fig. 6b with dashed lines.

To show the capability of the proposed direct method in adequately estimating the TQC, Fig. 6 also presents a comparison between the identified TQCs and reference (or expected) ones, shown as solid black lines. The reference $\beta_{diff}(\varepsilon)$ correspond to those used as input for the FE simulations serving as benchmarks. The reference $\beta_{int}(\varepsilon)$ matches the

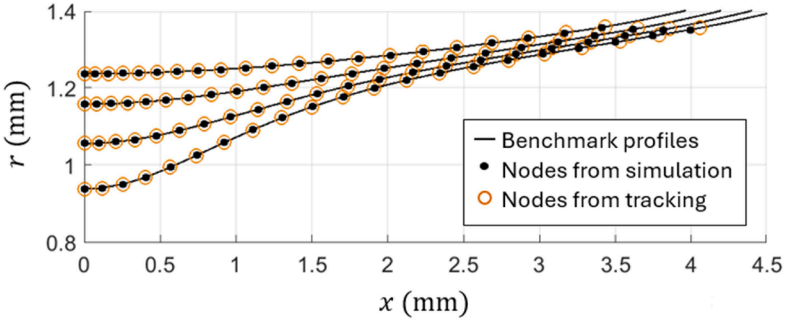


| $X_{max}$ (mm) | Error (%) |
|---|---|
| 2.50 | 0.29 |
| 2.30 | 0.24 |
| 2.1 | 0.21 |
| 1.9 | 0.19 |
| 1.7 | 0.19 |
| 1.6 | 0.19 |

**Fig. 4.** Application of the tracking technique for the case of variable TQC; the table indicates how the average error (computed with Eq. (6)) changes by varying $X_{max}$ (the maximum distance considered from the center of the sample in the undeformed configuration).

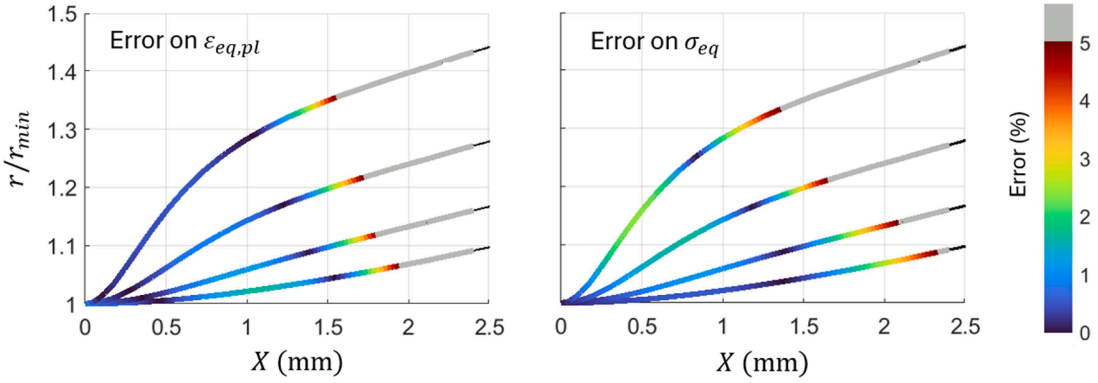


**Fig. 5.** Error maps of the Lagrangian strain and stress fields estimated with the database approach for the test with variable TQC.

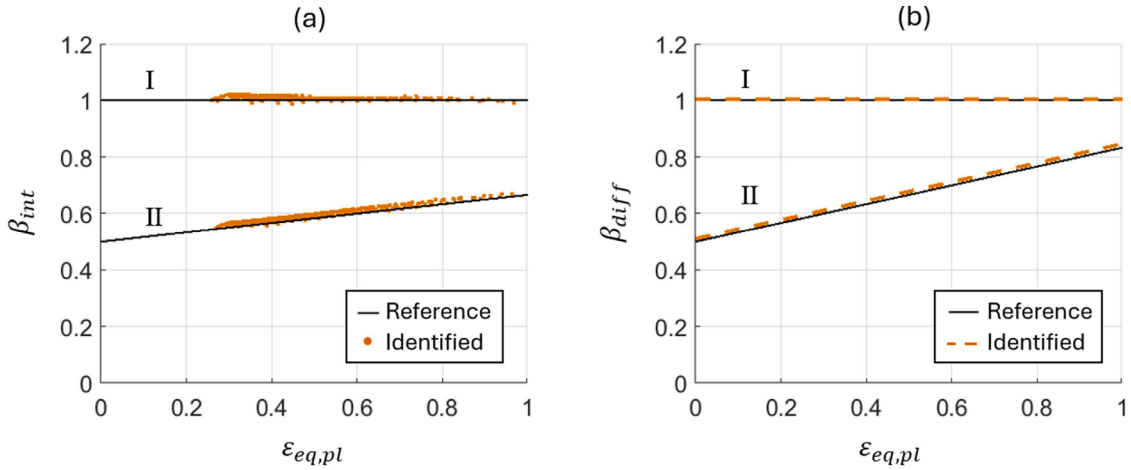


**Fig. 6.** Results of the proposed direct method on adiabatic tests, with constant TQC (case I) and strain-dependent TQC (case II); reference $\beta_{diff}(\varepsilon)$ is the one used as input in the FE simulation considered as benchmarks and the reference $\beta_{int}(\varepsilon)$ can be easily computed from it via Eq. (8).

reference $\beta_{diff}(\varepsilon)$ for case I, with constant TQC, whereas for case II, of variable TQC, $\beta_{int}(\varepsilon)$ was computed from the reference $\beta_{diff}(\varepsilon)$, according to the following relationship:

$$\beta_{int}(\varepsilon) = \frac{1}{\varepsilon}\int_0^{\varepsilon} \beta_{diff}(\tilde{\varepsilon})\, d\tilde{\varepsilon}. \tag{8}$$

A good agreement with these theoretical expectations can be observed in both the constant and strain-dependent TQC cases. Moreover, the fact that a wide region around the necking center is considered increases the reliability of the results compared to considering only the point at the surface center of the neck.

### 3.2. Iterative approach

Under non-adiabatic test conditions, heat loss phenomena other than plastic dissipation come into play, and properly accounting for them with a direct approach is not straightforward. For instance, to include heat conduction in a direct approach, it would be necessary to estimate the Laplacian of the temperature field (see Eq. (1)). However, temperature is measured only on the surface and not inside the specimen. To avoid introducing assumptions about internal temperature distribution, the authors propose using an approach based on thermo-mechanical FE simulations.

Mechanical and thermal phenomena are known to be strongly coupled: the mechanical response is affected by temperature rise, that is caused both by heat transfer and by self-heating, which in turn depends on the mechanical response itself. Due to such strong coupling, inverse methods for material characterization become more computationally expensive as it would be necessary to simultaneously identify mechanical response and heat conversion. As discussed in Section 1, a common approach at low strain rates is to treat thermal and mechanical behaviors as uncoupled, i.e., the temperature rise is not supposed to significantly affect the mechanical response. In this case, the mechanical response is identified with an arbitrary TQC, and this mechanical model is subsequently used to determine the actual TQC by analyzing the temperature field. This approach is reasonable if temperature increases are limited. However, at higher strain rates, especially for materials with low thermal conductivity, the temperature rise may be significant, and uncoupled approaches may no longer be valid.

To address this limitation in an efficient way, the authors propose using a plastic flow identification strategy which can determine the mechanical response independently of the heat conversion and without assumptions about it. This method, presented in [38], is based on the database approach summarized in Section 2. Considering that the main evidence of thermos-mechanical coupling is that the stress experienced by material points depends on their temperature, what makes the method able to identify the mechanical response independently from heat conversion is that two distinct methods are used for estimating the stress (database approach) and the temperature (infrared imaging). More specifically, but very briefly, the Eulerian fields $\varepsilon_{eq,pl}(x)$, $\dot{\varepsilon}_{eq,pl}(x)$, $\sigma_{eq}(x)$, obtained from the database approach are combined with the Eulerian field $T(x)$ obtained from the infrared camera. The resulting point cloud $(\varepsilon_{eq,pl}, \dot{\varepsilon}_{eq,pl}, T, \sigma_{eq})$ represents the material response during the test considered. This point cloud can be further enriched with

analogous data obtained from tests performed at different loading speeds, thus covering a wider range of strain rates and self-heating levels (and consequently, temperatures). Finally, depending on the model that it is intended to input in FE simulations, a fit of this data is done. Once plastic behavior is established, an iterative approach can be implemented to determine the heat conversion alone. This significantly reduces computational cost compared to simultaneously optimizing mechanical and thermal behavior. The specific iterative strategy presented in this paper is based on some simplifying assumptions, as explained in Section 3.2.1. Section 3.2.2 presents how the proposed iterative method performs on numerical examples.

### 3.2.1. Heat conversion identification

In this section, a preliminary iterative strategy for identifying heat conversion is presented. An approximate approach was adopted, in which only conduction was considered as an additional heat loss mechanism beyond plastic dissipation, i.e. radiant and convective heat losses were neglected. While radiation is commonly neglected in literature, convection is sometimes considered. Hence, neglecting convective heat transfer with the surrounding air, implies that the proposed method is applicable to situations where this form of heat loss is negligible compared to conduction. Another simplifying hypothesis concerned thermal conductivity, which was considered constant through the tests, despite its potential variation due to temperature changes. Regarding the TQC, since there is experimental and theoretical evidence of its dependence on multiple variables, the proposed strategy should be capable of identifying a variable TQC. However, unlike direct methods, it requires defining in advance which variables are expected to influence the work-to-heat conversion. In this study, the TQC is modeled as a function of the equivalent plastic strain. This is an empirical approach aimed at capturing variations in TQC, without implying that strain alone governs the conversion process. In fact, any variable that evolves similarly to strain would be implicitly included in such TQC evaluation. Conversely, since strain rate does not evolve proportionally to strain during necking, the effect of strain rate variations within a single test is neglected in the proposed strategy.

Based on these assumptions, the authors implemented an iterative strategy, schematically illustrated in Fig. 7, which was observed to converge in a few steps, as will be shown in Section 3.2.2. The method consists of running a FE simulation using a trial TQC and a given thermal conductivity and extracting the resulting temperature distribution $T_{FE}(x)$ at a highly deformed configuration. This distribution is then compared with the experimental one $T_{EXP}(x)$. In this approach, the difference between them is attributed to the TQC. Specifically, the ratio between experimental and numerical temperature increments (relative to room temperature) is used as a correction factor $k_\beta(x) = \Delta T_{FE}/\Delta T_{EXP}$ of the trial TQC. To obtain a strain-dependent correction factor $k_\beta(\varepsilon_{eq,pl})$, the association $\varepsilon_{eq,pl}(x)$ is established via the FE simulation (provided that the numerical necking profile closely approximates the experimental one). The updated TQC is then input in a new simulation, which in turn produces the next trial. This procedure is iteratively repeated until an acceptable error is achieved in the temperature prediction. Preliminary investigations showed that this guided strategy is much more efficient than performing an optimization where the trials of TQC are not well-guided. Finally, the procedure focuses just on a single highly deformed configuration because different points on the specimen surface experience various strain values simultaneously. Earlier configurations would provide mostly redundant information. Therefore, if a simulation using the identified TQC can also accurately reproduce the temperature distribution at other configurations, it suggests that heat conversion has been properly modeled. If not, it would indicate that some relevant variables are missing from the model, and further investigation would be necessary.

Overall, this method should be conceived as a preliminary proposal, based on an approximate modelling of heat losses and a tentative procedure for iterating. Nevertheless, it already shows strong potential, as will be highlighted by the numerical and experimental applications in Sections 3.2.2 and 4.2 respectively.

### 3.2.2. Numerical examples

In this section, ad-hoc numerical benchmarks are presented with the aim of showing that the developed iterative strategy quite rapidly converges to the expected result. To focus only on the optimization strategy, the benchmarks satisfied the hypotheses previously discussed, the heat conduction was supposed to be known and the plastic flow curve to be correctly identified.

The same FE model described in Section 3.1.2 was used. To simulate scenarios in which heat conduction significantly influences the specimen's temperature, low strain rate tests were considered. The specific test speed at which conduction becomes relevant depends on the

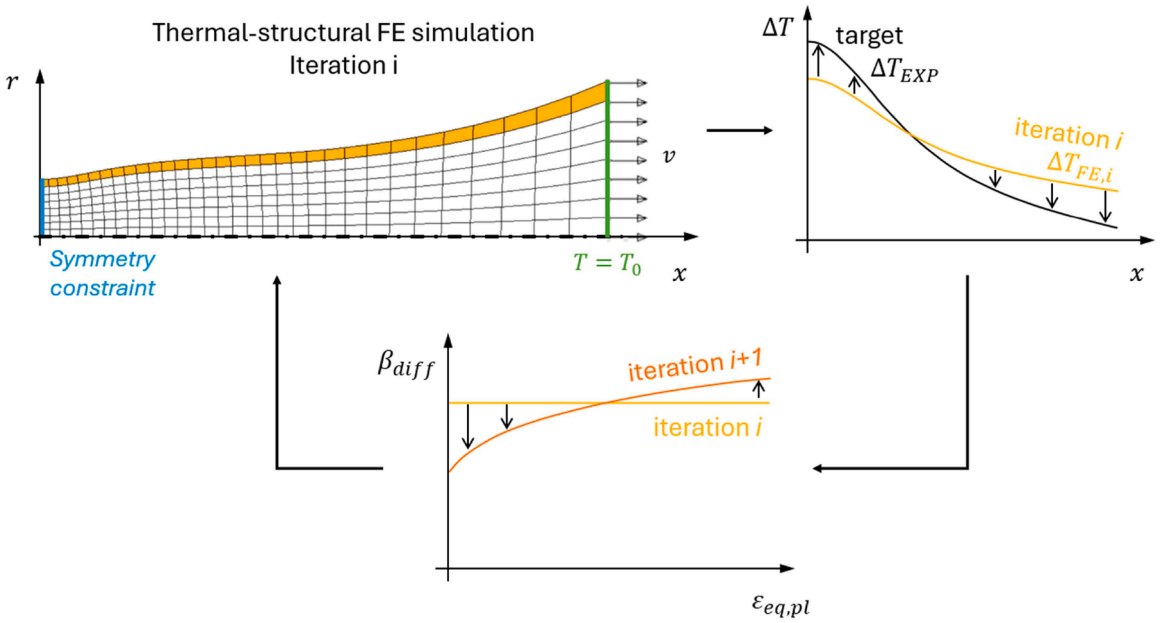


**Fig. 7.** Schematic representation of the iterative approach; the colored elements of the FE model are those considered for extracting $\Delta T_{FE,i}(x)$.

material's thermal diffusivity [44]; for the case under study, it was found that a nominal strain rate of 1 $s^{-1}$ served as a suitable example. A constant thermal conductivity of 76.1 W/(m·K) was used because, as long as heat capacity is assumed to be known, introducing a thermal dependence of would not have a meaningful impact. Convective and radiative heat losses were not considered, as anticipated in Section 3.2.2. Regarding the TQC, only the case of a strain-dependent TQC is presented as it represents a more general condition than that of a constant TQC. Coupled thermal-structural simulations were run, using the explicit solver for the structural response and the implicit solver for the thermal one. In addition, a nominal strain rate of $10^2$ $s^{-1}$ was also analyzed to represent adiabatic conditions. It was verified that, for the Armco Iron material model, heat conduction has a negligible effect at this strain rate. This example aims to emphasize the versatility of the technique, which is applicable to both adiabatic and non-adiabatic conditions.

The above simulations were used as benchmarks. For each case, the temperature distribution at a highly deformed configuration was selected, and the proposed iterative strategy was applied.

The tables shown in Fig. 8 summarize the temperature prediction error across successive iterations. At each iteration, the error was computed using temperature distributions at several necking configurations and the following expression:

$$error = \mathrm{RMSE}\left(\frac{\Delta T - \Delta\widetilde{T}}{\Delta T}\right), \tag{9}$$

where RMSE denotes the Root Mean Square Error, $\Delta T$ is the reference temperature increment and $\Delta\widetilde{T}$ is the temperature increment at the current iteration. Some TQC trials from various iterations are shown in Fig. 8 too (only some iterations are displayed for clarity).

These plots and tables show that both the trial TQCs and the resulting temperature distributions converged closely to the reference and expected values. This is better shown in the plots on the right side, which compare temperature distributions at the first and at the last iteration with reference data. Such plots also depict that adjusting the TQC to match a single temperature distribution resulted in accurate predictions of earlier configurations as well. This was possible because the most deformed configuration, which experienced the wider range of strains, already contained sufficient information. A strain dependence of the TQC different from the one identified could lead to the same maximum temperature but would not guarantee the same temperature distribution. These considerations hold true for both adiabatic and non-adiabatic conditions. Accurate results were achieved in both scenarios, underscoring the general applicability of the proposed technique. Furthermore, the difference in the shape of the temperature distributions between the two benchmarks is noteworthy: at lower strain rates, conduction plays a more significant role, causing the temperature to be less localized compared to adiabatic conditions.

Overall, the results suggested that, despite its preliminary form, the proposed iterative strategy has great potential, which encouraged applying it to an experimental case study, as discussed in the next section.

## 4. Experimental case study

The proposed methodologies, after being validated through numerical benchmarks, were applied to investigate the work-to-heat conversion in tensile tests presented in [38]. The material studied was 17–4PH martensitic stainless steel (H900), which exhibits moderate sensitivity to

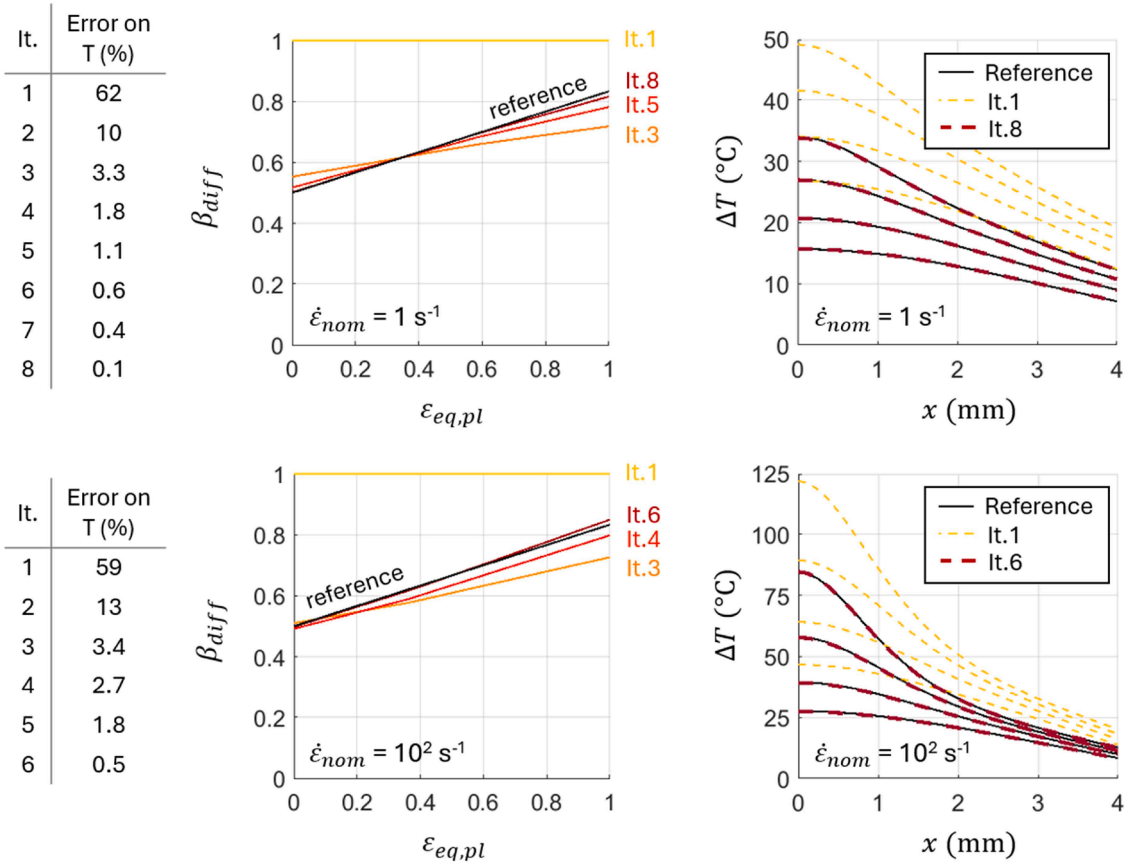


**Fig. 8.** Results of the proposed iterative approach on a virtual material with variable TQC in case of a test under non-adiabatic conditions ($\dot{\varepsilon}_{nom}$ of 1 $s^{-1}$, top part of the figure) and of a test under adiabatic conditions ($\dot{\varepsilon}_{nom}$ of $10^2$ $s^{-1}$, bottom part of the figure). The error on temperature reported in tables is computed according to Eq. (9).

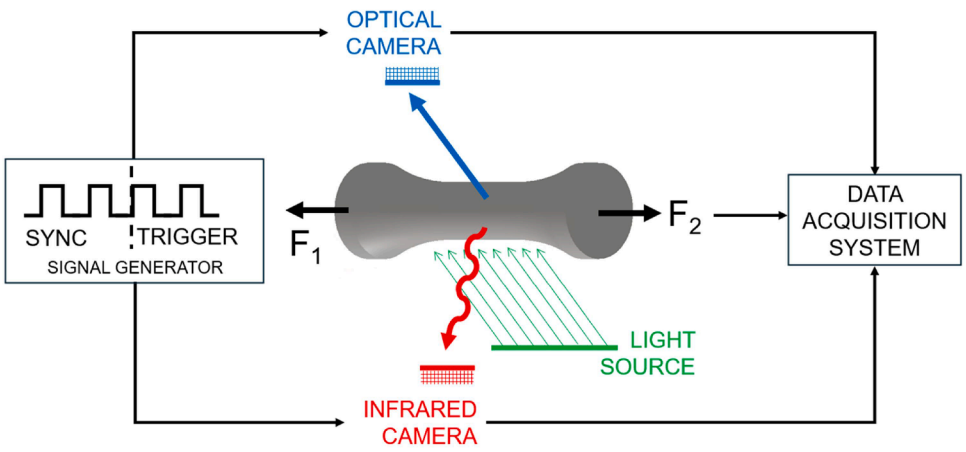


**Fig. 9.** Schematic representation of the experimental setup.

strain rate and tends to undergo considerable self-heating due to its low thermal conductivity. Cylindrical dog-bone specimens with threaded ends, a gauge length of 5 mm and a gauge radius of 3 mm were obtained by turning a previously treated round bar. Tests were performed at room temperature and at various strain rates. This paper focuses on tests conducted at nominally 1, 10, and $10^3$ $s^{-1}$, where a significant temperature rise was observed. Tests at the two lower strain rates were carried out on a Dartec-HA100 servo-hydraulic testing machine. In contrast, the higher strain rate condition was achieved with a Split Hopkinson Tension Bar (SHTB) in direct configuration (see Scapin et al. [45] for a detailed description). All tests were recorded using high-resolution, high-speed optical and infrared cameras. The infrared imaging was performed with a FLIRX6900sc SLS camera. Different optical cameras were employed depending on the test speed. For the servo-hydraulic machine tests, a Photron Mini AX50 captured the full specimen shape at 500 and 5000 fps for tests at nominal strain rates of 1 and 10 $s^{-1}$, respectively. For the SHTB tests, both a Photron FASTCAM SA5 and a Photron FASTCAM Nova S6 were employed. The Photron FASTCAM SA5 was able to record the entire specimen shape at a maximum frame rate of 50,000 fps. To achieve higher frame rates necessary for monitoring the minimum radius, a second camera, the Photron FASTCAM Nova S6, was used. By cropping the image to focus on a smaller region around the minimum cross-section, this camera was able to reach an acquisition rate of 100,000 fps.

As schematically illustrated in Fig. 9, the optical and infrared cameras were positioned at an angle of approximately 90° relative to each other. It was verified that the light source, placed opposite to the optical camera to enable backlight images, did not interfere with the thermal measurements. The fact that the optical and infrared cameras were viewing different sides of the specimen did not pose a problem under the assumption of axial symmetry underlying the entire procedure.

The ideal configuration for image acquisition would involve synchronous and simultaneous recording of visible and infrared images. This was achieved during the tests at low-medium strain rates, but not at high strain rates. A detailed explanation of this limitation, along with considerations regarding temperature measurements, is provided in Section 4.1. In addition, Section 4.1 also describes how infrared images were post-processed to extract temperature distributions. The work-to-heat conversion during the different tests is then investigated using the proposed methods in Section 4.2.

### 4.1. Thermal data acquisition and analysis

Experimentally measuring temperature is a key aspect of the proposed method. Infrared imaging was chosen because it enables full-field temperature acquisition. However, infrared camera technology still has significant room for improvement, as thoroughly discussed by Soares et al. [30]. Despite recent advancements, current acquisition rates remain lower than those of modern high-speed optical cameras, which hinders the potential of simultaneous optical and infrared imaging.

A crucial parameter in infrared cameras is the integration time, which must be appropriate for capturing the time evolution of the observed phenomenon. For fast thermal events, a shorter integration time would be preferable to catch instantaneous temperature; otherwise, the detected temperature represents an average of the real temperature over the integration time. This effect is particularly important when recording a body that is simultaneously heating and moving (as in tensile tests), since motion causes spatial averaging as well. This phenomenon is analogous to motion blur in photography. The shorter the integration time, the lower this effect becomes. However, the integration time must also be long enough to allow sufficient infrared radiation (i.e., emitted photons) to reach the camera sensor. The camera's sensitivity is inherently limited by the amount of radiation emitted by the specimen at a given temperature. While short integration times are feasible for high-temperature measurements (where more photons are emitted), they are challenging in near-room-temperature experiments. Indeed, reducing integration time in such cases can prevent reliably measuring low temperatures. In the tests presented in this work, temperatures above 300 °C were reached during necking, but the specimens were initially at room temperature. Hence, selecting the integration time required balancing the need to measure low temperatures accurately and to follow the high-speed deformation. An integration time of 50 μs was chosen for all tests.

Regarding acquisition rates, these were limited by the spatial resolution required by the proposed method. Synchronous visible and infrared acquisition was possible in low-medium strain rates tests; acquisition rates of 500 and 5000 fps were used for tests at 1 and 10 $s^{-1}$ respectively. Fig. 10 shows some sample configurations during a test at nominally 10 $s^{-1}$ by graphically coupling infrared and optical images. In high strain rates tests, higher frame rates were necessary. At the required spatial resolution, the optical camera used for recording the whole shape could reach 50,000 fps, while the infrared camera could attain only 16,040 fps (with an image of size 16 × 640 pixels). Hence, synchronous and simultaneous acquisition would have required reducing the optical camera's rate. Instead, the authors opted to use the maximum acquisition rates for both cameras. As a result, fewer infrared frames were captured, and they were not recorded at the exact same times as the optical frames. However, since both systems were triggered by the same signal, a shared time reference was maintained. Given that the integration time resulted to be relatively long for high strain rate tests, infrared images were temporally located at the center of the integration window.

Another important aspect is that, when determining radiometric temperature, infrared technology typically assumes that the target

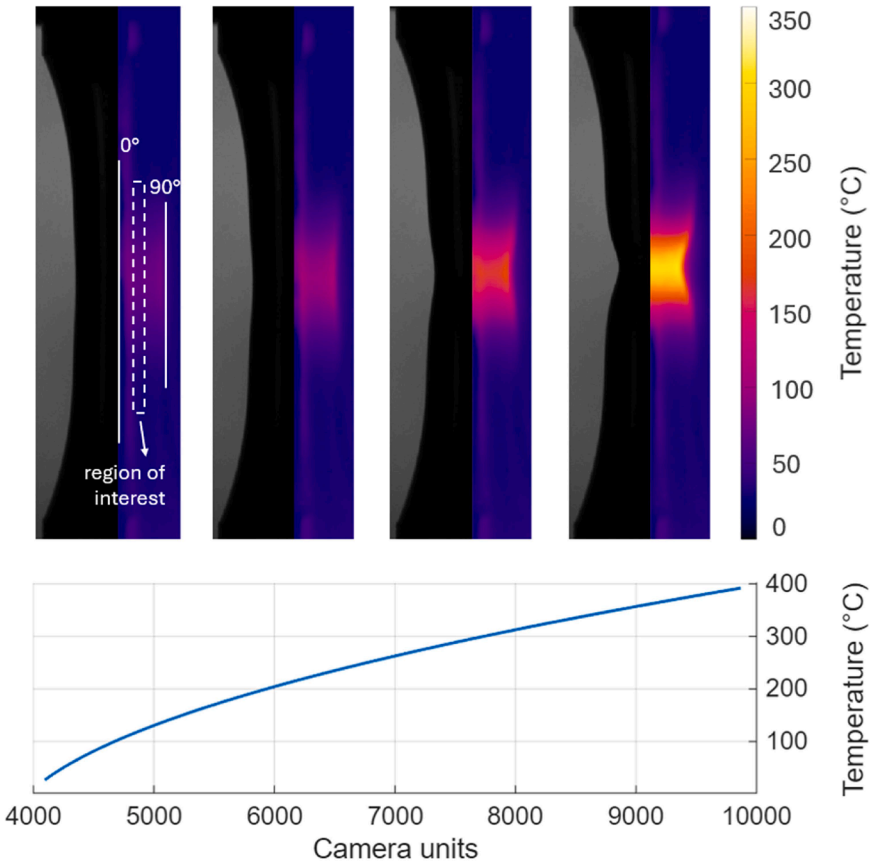


**Fig. 10.** Optical and infrared images acquired during a test at nominally 10 $s^{-1}$. In the first image, the region of interest considered for the analyses is shown together with the boundary observation angles of the infrared camera. The plot at the bottom shows the calibration curve used.

surface has the emissivity of a black body. Since this assumption is generally inaccurate, especially for metals, a coating is sometimes applied to increase the surface emissivity (for example, as one by Salehi and Kingstedt [46]). However, the coating must adhere perfectly to the material surface throughout the process, which could be unfeasible during necking [36]. Thus, the method adopted in this study involved converting the measured radiometric temperatures to actual surface temperatures using calibration curves (as done in the works [9,36,37]). Specifically, a single calibration curve was determined, ensuring that for all tests camera settings, distance between the camera and the sample, and viewing angle matched those used during calibration. Calibration was performed by heating the specimen with an induction system and then monitoring its cooling using both thermocouples and the infrared camera. The resulting calibration curve (specific to material, experimental setup, and camera setting) is shown in Fig. 10.

Finally, it is also worth mentioning that, although changes in surface roughness during plastic deformation can affect emissivity, studies have shown that the influence of deformation and surface finish on metal emissivity is relatively small [3,36,47].

Infrared images were post-processed to extract the temperature distribution along the specimen's surface in the axial direction. Theoretically, in the case of axial symmetry, all pixels aligned along the axial direction should yield the same temperature distribution. Full-field image improves redundancy and allows for averaging distributions obtained from different sets of pixels aligned with the axis. However, during this phase, care must be taken to exclude lines affected by light reflections, which act as outliers. Moreover, the observation angle of the infrared camera varies along the specimen surface. As shown in the first image of Fig. 10, the midline of the specimen in the image corresponds to an observation angle of 0°, which increases to 90° at the specimen's boundary. This boundary remains at a 90° observation angle throughout the test, while other points are characterized by varying angles due to necking. High observation angles are known to affect apparent emissivity. Hence, to avoid the effects of both reflection and high observation angles an adequate region (as shown in Fig. 10, for example) was identified and used for analysis.

Because the approach focuses on a semi-profile, only half of the average temperature distribution was considered. At medium-low strain rates, the midpoint can be identified either by overlapping the silhouette from the visible and the infrared images or by locating the maximum of the temperature distribution. At high strain rates, however, the infrared images were cropped to achieve high frame rates, preventing the silhouette from being visible. In these cases, the midpoint was identified as the point of maximum temperature. Tests at lower strain rates showed that both methods yielded nearly equivalent results. Finally, in all tests, the temperature semi-profile chosen corresponded to the part of the specimen moving more slowly. Fig. 11 shows some temperature semi-profiles for different tests at various nominal strain rates. For each configuration, the profiles plotted with thicker lines represent the average temperature distribution across six different pixel lines from the infrared image (individual distributions, plotted with dashed lines in Fig. 11, are not always visible due to overlapping with the average). To enable comparison across tests, the configurations were selected such that the maximum strain achieved on the surface was approximately the same. The values of strain, shown next to each configuration, were determined using the database approach.

The plots of Fig. 11 show that, as expected, the temperature achieved in a test at 1 $s^{-1}$ was lower than in a test at 10 $s^{-1}$. This can be mainly due to heat conduction, which has more time to develop in tests conducted at lower speeds. In addition, the positive strain rate sensitivity of the material may also imply that the plastic work done on material points is lower at lower speeds. The test at nominally $10^3$ $s^{-1}$ only partially

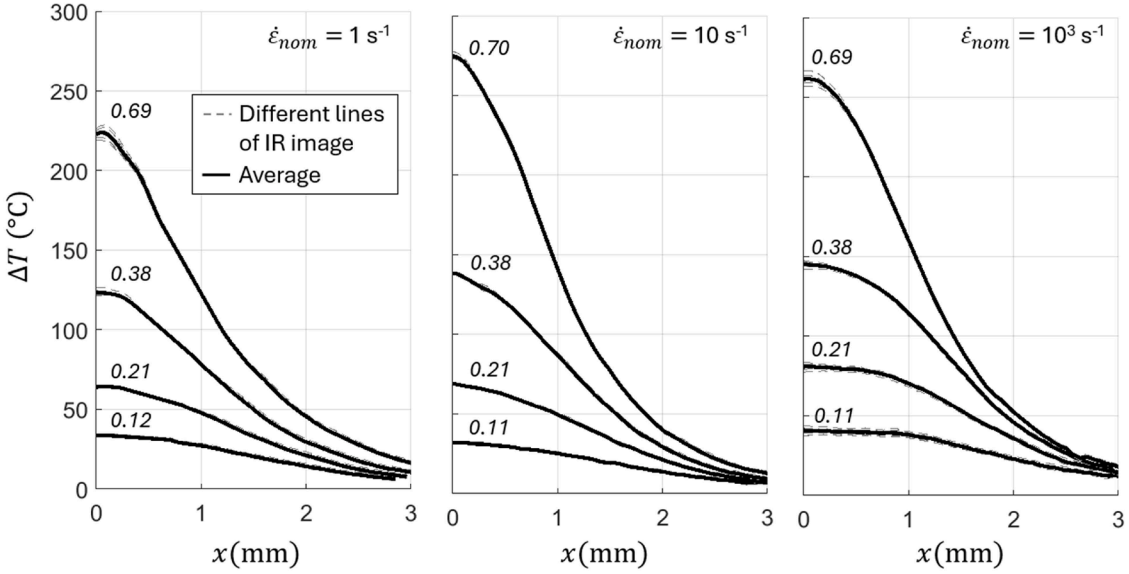


**Fig. 11.** Temperature distributions recorded during tests at different nominal strain rates. Next to each configuration the corresponding maximum superficial $\varepsilon_{eq,pl}$ is written.

confirms this observation. The configurations at lower strain levels were characterized by a higher temperature with respect to the corresponding configurations of the other tests. However, the final configuration showed a lower peak temperature and a less localized temperature distribution, compared to the 10 s$^{-1}$ test, despite the expectation that adiabatic conditions would enhance localization at higher strain rates. Nevertheless, it is important to note that temperature measurements in tests at nominally 10$^3$ s$^{-1}$ are subject to greater spatial and temporal averaging. This is due to the combined effects of the infrared camera's integration time and rapid motion of the specimen. Improvements in temperature measurement during high strain rate tests could be achieved by reducing the integration time, though this would come at the cost of lower sensitivity near room temperature.

### 4.2. Work-to-heat conversion

The temperature distributions determined as described in the previous section were used to investigate the work-to-heat conversion using both the proposed direct and iterative methodologies. In this section, results are reported for one test at each nominal strain rate. To minimize the influence of ductile damage, the analysis focused on the phase of the tests that was sufficiently distant from significant reductions in mechanical strength.

To apply the direct method, the Eulerian temperature field (obtained from infrared imaging) and the Eulerian fields $\varepsilon_{eq,pl}(x,t)$ and $\sigma_{eq}(x,t)$ (obtained with the database approach, starting from load history and necking semi-profiles extracted from optical images) were converted into Lagrangian fields. This conversion was made possible through the developed tracking strategy (see Section 3.1.1). Fig. 12a shows the deformation paths of different material points for the tests at nominally 10 s$^{-1}$. These material points, denoted with capital letters (from A to G), are represented with different colors. Their positions on the sample surface at different times are shown in Fig. 12b. At each time, every point is in a specific state $(\varepsilon_{eq,pl}, \sigma_{eq})$ which is indicated on the plot of Fig. 12a. Each marker shape (square, triangle, circle, diamond) in Fig. 12a corresponds to one of the configurations illustrated in Fig. 12b. The various paths progressively deviate from that of the profile center, as expected in the presence of strain rate sensitivity within a single test due to necking [38].

The evolution of plastic work was then evaluated for the different material points. However, points farther from the neck were excluded from the analysis, as they could be influenced by the dog-bone geometry (as shown in Section 3.1.2). Finally, Eq. (4) was applied to the selected material points, yielding to a series of points $\beta_{int}(X,t)$. When applying Eq. (4), both the material density and specific heat must be considered. In the present analysis, constant values of 7800 kg/m$^3$ and 460 J/(kg·K)

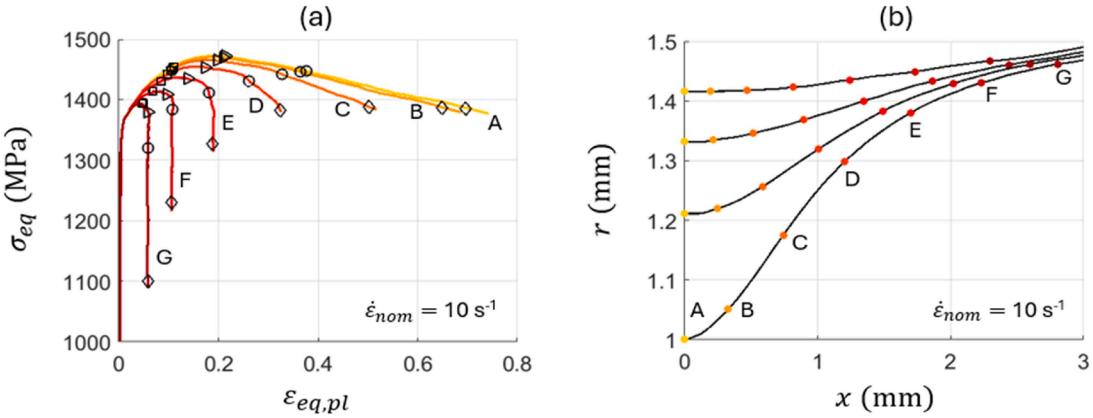


**Fig. 12.** Deformation paths of various material points (a) and their position on the specimen's surface (b) at different configurations for a test at nominally 10 s$^{-1}$.

were used, neglecting the temperature dependencies of these properties. As a result, the identified TQCs implicitly account for the temperature dependencies of these variables. Moreover, in tests where adiabatic conditions are not met, the results yield an apparent TQC which also reflects the influence of heat conduction. These results are still reported and should be interpreted as an empirical approach where the apparent TQC implicitly models the combined effects of self-heating and heat conduction.

Fig. 13 collects the results of applying the direct method to the three tests in terms of both integral and differential TQC. Since the direct approach provides the integral TQC as a point cloud, the authors decided to analyze it as a function of equivalent plastic strain and to fit it with a mathematical law. The resulting $\beta_{int}(\varepsilon_{eq,pl})$ curves are shown as dashed lines in Fig. 13a, with different colors corresponding to different tests. Then, Eq. (7) was used to determine $\beta_{diff}(\varepsilon_{eq,pl})$, which are plotted as dashed lines in Fig. 13b.

To apply the iterative approach, which allows better accounting for non-adiabatic conditions, coupled thermal-structural simulations were used. From the mechanical perspective, the plastic flow curve input in the simulations was identified by the authors in [38] under self-heating conditions, following the procedure described in Section 3.2. Specifically, a model with multiplicative uncoupling of strain, strain rate and temperature was found to yield good results; detailed information could be found in [38]. Then, the iterative strategy based on comparing temperature distributions at a highly deformed configuration was applied to determine the heat conversion. On the thermal side, a simplified approach was used: a constant thermal conduction coefficient optimized for the test configuration was considered (10 W/(m·K)) and also the density and the specific heat were considered to be constant (as done in the direct approach). The results of the iterative method are shown as continuous lines in Fig. 13. Since this approach provides the differential TQC, the corresponding integral TQC was obtained using Eq. (8).

In Fig. 13, each line is plotted only over the range of strains reached during the tests, from the necking onset up to the final considered configuration. This illustrates how focusing on the post-necking phase enables investigation up to large strains.

The direct and the iterative methods produced comparable results for the test at nominally $10^3$ $s^{-1}$ since this condition can be reasonably considered adiabatic. This was also verified by evaluating the Fourier number *Fo*, defined as:

$$Fo = \frac{\alpha t}{L^2}, \tag{10}$$

where $\alpha$ is the thermal diffusivity, $t$ the test duration, and $L$ the characteristic length through which conduction occurs. By considering half the initial gauge length as characteristic length, a value of $Fo_L \approx 2{\cdot}10^{-4}$ was obtained. Since this is much lower than the commonly accepted threshold of $10^{-2}$, the process can be considered essentially adiabatic [48].

At the nominal strain rate of 10 $s^{-1}$, $Fo_L \approx 1{\cdot}10^{-2}$ which lies at the boundary of adiabaticity. Moreover, given that the hottest point during necking is located at the specimen's minimum cross-section along its axis, heat conduction occurs not only axially but also radially. Hence, the Fourier number was also calculated using the initial gauge radius as characteristic length, resulting in $Fo_R \approx 4{\cdot}10^{-2}$. This suggests that the process is not fully adiabatic, which helps explain the small discrepancies observed between the direct and the iterative methods for the test at nominally 10 $s^{-1}$.

For the 1 $s^{-1}$ test, a larger discrepancy between the two methods was found, as expected due to more pronounced conduction at lower strain rates. In this case, $Fo_L \approx 1{\cdot}10^{-1}$, indicating that the process was neither adiabatic nor isothermal, but significantly affected by thermal conduction.

Regarding the strain dependence of the work-to-heat conversion, one should focus on the results of the iterative approach. This is because, as previously noted, the direct approach provides only apparent TQCs in non-adiabatic conditions. At a nominal strain rate of 1 $s^{-1}$, a TQC was found to increase with plastic strain. This is consistent with findings from previous studies, such as Smith et al. [37] on a titanium alloy, Dæhli et al. [34] on DP steels and aluminum alloys and Lew et al. [12] on austenitic stainless steel. A similar trend was observed for the 10 $s^{-1}$ test, although in this case the work-to-heat conversion appeared to saturate beyond 20 % plastic strain. For the higher strain rate test, the TQC remained nearly constant with strain or slightly decreasing. However, as already noted, this last test involved temperature measurements that were more averaged in time and space due to the combined effect of integration time and specimen's motion. This may explain the apparent decrease in differential TQC at higher strains. Improvements could be obtained by reducing the integration time, but with the drawback of low sensitivity near room temperature. Moreover, it is important to stress that an empirical approach was adopted and, even though a $\beta(\varepsilon_{eq,pl})$ was identified, this may implicitly capture the effects of other variables (e.g., temperature dependencies of thermal conductivity and specific heat, temperature dependence of TQC, etc.). As with any empirical approach, caution must be exercised when attempting to extract physical meaning. For example, by comparing the results across strain rates, the TQC seems to depend on strain rate too, an effect already acknowledged in

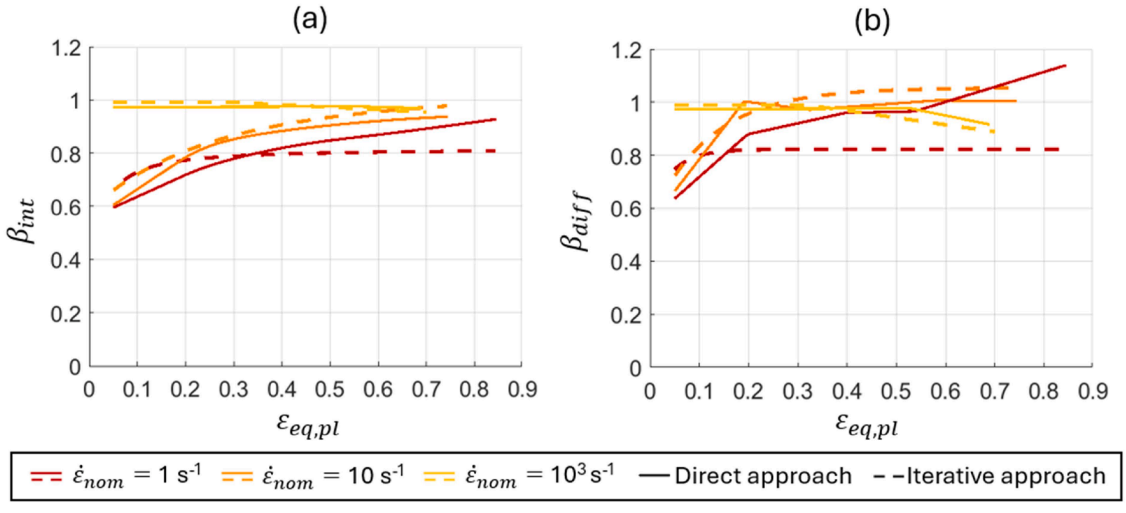


**Fig. 13.** Differential and integral TQC according to both the direct and the iterative approach for three different nominal strain rates.

literature for certain materials. However, further investigation is required in this case, particularly since the strain rate also varies within a single test due to necking.

Because empirical methods identify TQCs that, depending on the method's assumptions, inherently model physical phenomena different from self-heating (e.g., heat conduction), it cannot be guaranteed that temperature distributions at all configurations are adequately predicted. Hence, the temperature distributions numerically predicted using the different identified TQCs were compared to the experimental distributions, as shown in Fig. 14. For the iterative approach, the distributions were readily available from the final iteration and are plotted as solid black lines. Conversely, for the direct approach, adiabatic FE simulations were run for all tests since, as previously mentioned, the apparent TQCs inherently accounted for heat conduction. The material model describing the plastic behavior was taken from [38]. The resulting temperature distributions are shown in Fig. 14 as dashed black lines.

These results show that the iterative approach led to accurate predictions across all tests analyzed. In contrast, the direct method produced very good results only for the test at nominally $10^3$ $s^{-1}$, a slight discrepancy was observed at 10 $s^{-1}$, while a more significant error was found at the lower strain rate. This is probably due to heat conduction: it is limited at 10 $s^{-1}$ but becomes relevant at 1 $s^{-1}$. Nevertheless, the results at 10 $s^{-1}$ suggest that an apparent TQC can still represent the effects of heat conduction through appropriate strain dependence. At 1 $s^{-1}$, however, the longer time available for heat conduction prevents it from being effectively modeled through a strain-dependent TQC. In this case, only the iterative approach, which employs thermal-structural FE simulations, was able to properly account for heat conduction. Moreover, even in the test at 10/s, where the direct method already performed well, the iterative method offered additional insights. In particular, it enabled the separation of heat conduction effects in the evaluation of the TQCs, as illustrated in the plots of Fig. 13. Despite the use of an approximate thermal model, the iterative method provided an improved description of the temperature fields.

Furthermore, it is important to underline that, although the target of the iterations was only the most deformed configuration in each test, the other configurations were also accurately predicted, as shown in Fig. 14. This suggests that modeling TQC as a function of strain effectively captures experimental behavior. Nevertheless, this does not imply that strain is the only governing variable, as other factors varying in a similar way during the test may also play a role.

As expected, the iterative method outperformed the direct one for the test at the lowest strain rate. Conversely, the direct approach may be more convenient at the highest strain rate due to its lower computational cost. In the remainder of the analysis, only the iterative approach was considered for the lowest strain rate, only the direct approach for the highest, and both methods were used for the intermediate strain rate. It is important to compare numerical predictions with experimental data in terms of necking profiles and engineering stress vs. radial contraction curves. The good agreement that is visible from Fig. 15 confirms that the coupled thermo-mechanical behavior associated with self-heating during necking was well captured by the models.

## 5. Conclusions

The present paper focused on the post-necking phase of tensile tests to investigate the work-to-heat conversion up to large strains with a phenomenological approach.

The first method presented in the paper directly employs the heat equation to estimate the TQC and applies only under adiabatic conditions. A key development was the technique for tracking material points in case of backlight optical images. This enables adopting a Lagrangian perspective on several material points during the analysis of work-to-heat conversion, while also benefiting from high-contrast images thanks to backlighting. The accuracy of the tracking technique was verified through numerical benchmarks, which also confirmed the overall feasibility of the method under adiabatic conditions.

For non-adiabatic cases, the authors proposed an iterative approach based on thermal-structural FE simulations. It involves recursively adjusting the TQC by comparing experimentally measured and numerically predicted temperature distributions at a single, highly deformed configuration. A notable feature of this approach is that it focuses exclusively on determining heat conversion. Indeed, the plastic flow curve was suggested to be identified using the database approach, which allows plastic flow identification independently from the determination of the work-to-heat conversion. Only in a subsequent step are mechanical and thermal data combined to investigate the conversion of plastic work into heat. Nevertheless, the specific iteration strategy should be considered a preliminary proposal. An approximate approach was adopted in considering only conduction with constant thermal

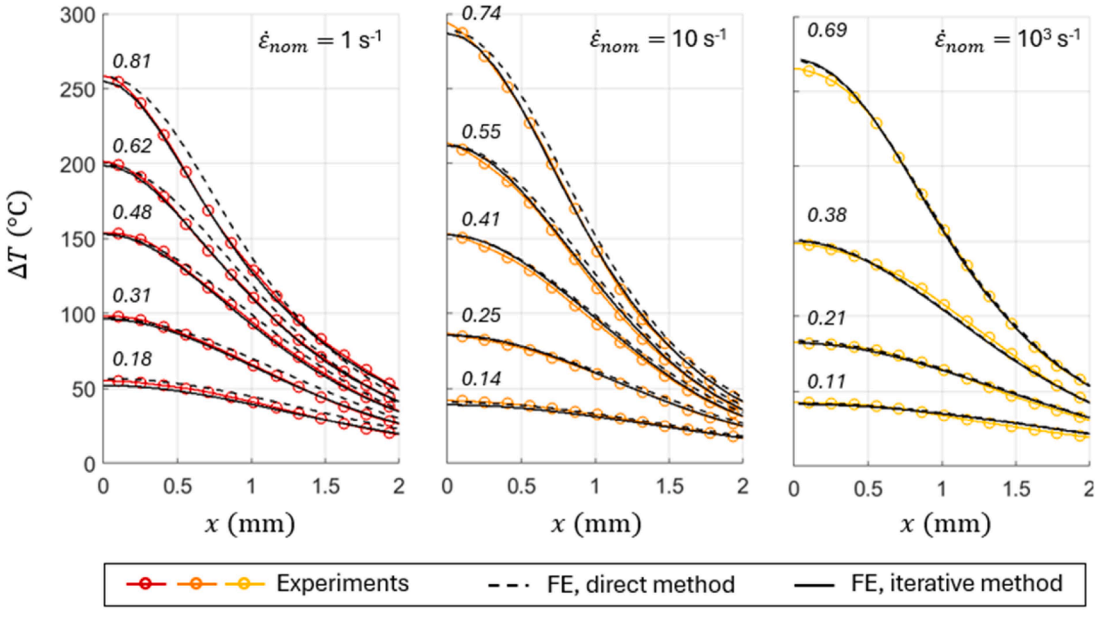


**Fig. 14.** Comparison of temperature distributions between experimental results and numerical predictions. Next to the temperature distributions the corresponding maximum superficial $\varepsilon_{eq,pl}$ is written.

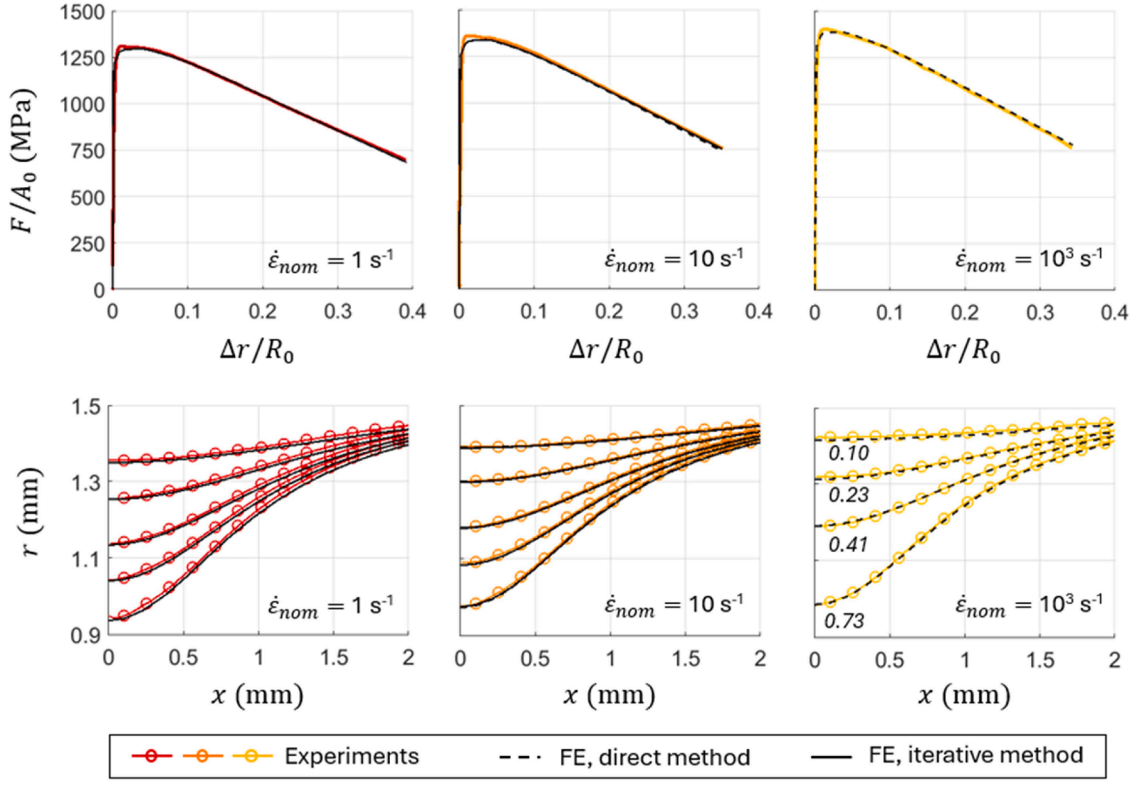


**Fig. 15.** Comparison between experimental results and numerical predictions in terms of necking profiles and engineering stress vs. radial contraction at the minimum cross-section. The maximum superficial $\varepsilon_{eq,pl}$ at each necking configuration is the same of Fig. 14 for $\dot{\varepsilon}_{nom}$ of 1 $s^{-1}$ and 10 $s^{-1}$, whereas for $\dot{\varepsilon}_{nom}$ of $10^3$ $s^{-1}$ is written on the plot, since it is different from Fig. 14.

conductivity as additional heat loss to plastic dissipation. Since numerical benchmarks suggested the potential of the proposed approach in this simplified form, the method seems worthy of future attention for further improvements.

Finally, both methods were applied to experimental case studies. The strain analysis effort is significantly lower compared to DIC on cylindrical specimens during advanced necking, as the proposed approaches focus simply on analyzing the necking silhouettes from backlit images. Conversely, the current form of this approach has the limitation of being applicable only to round samples of isotropic materials. From the thermal perspective, the experimental setup required careful attention and trade-offs to obtain reliable thermal data with adequate time and spatial resolution. In this regard, future work may focus on improving infrared image acquisition at high strain rates to mitigate motion blur. Nevertheless, this limitation did not prevent comparison of the two methods across different tests. At higher strain rates, where adiabatic conditions were met, both methods produced comparable results. At a nominal strain rate of 10 $s^{-1}$, heat conduction began to affect the outcomes, resulting in slight discrepancies between the two approaches. For the 1 $s^{-1}$ tests, conduction effects were more pronounced, and only the iterative method accurately predicted the temperature distributions by identifying an appropriate TQC. In conclusion, the results demonstrate the practical applicability of the proposed methods which proved capable of determining an experimentally informed TQC up to strains above 70 %. The direct method is more computationally efficient, while the iterative approach is more general and shows promising results, despite being in its preliminary stage.

## CRediT authorship contribution statement

**Marta Beltramo:** Writing – review & editing, Writing – original draft, Visualization, Validation, Software, Methodology, Investigation, Formal analysis, Conceptualization. **Martina Scapin:** Writing – review & editing, Validation, Supervision, Resources, Methodology, Investigation, Conceptualization. **Lorenzo Peroni:** Validation, Supervision, Resources, Project administration, Methodology, Investigation, Conceptualization.

## Declaration of competing interest

The authors declare that they have no known competing financial interests or personal relationships that could have appeared to influence the work reported in this paper.

## Appendix A

Consider a cylinder of radius $R_0$, each cross-section in the undeformed state will be denoted with coordinate $X$. In the deformed state, the cross-sections become curved, and the coordinate of their average axial position is denoted by $\Lambda(X)$. The stretch is then defined as $\lambda(X) = \frac{d\Lambda}{dX}$.

Referring to Audoly and Hutchinson's 1D theory and considering the material isotropic and incompressible, for the 2D axisymmetric problem, the deformed coordinates $(x, r)$ of a point of initial coordinates $(X, R)$ become:

$$x(X,R) = \Lambda(X) + \frac{1}{4\,\lambda(X)^3}\frac{d\lambda(X)}{dX}\left(R^2 - \frac{R_0^2}{2}\right), \tag{A.1a}$$

$$r(X,R) = \frac{R}{\sqrt{\lambda(X)}}, \tag{A.1b}$$

where the terms of higher order have been neglected.

Since the present analysis focuses on points on the specimen surface, for which $R = R_0$, previous Eq. (A.1) becomes:

$$x(X) = x(X,R_0) = \Lambda(X) + \frac{1}{4\,\lambda(X)^3}\frac{d\lambda(X)}{dX}\frac{R_0^2}{2}, \tag{A.2a}$$

$$r(X) = r(X,R_0) = \frac{R_0}{\sqrt{\lambda(X)}}. \tag{A.2b}$$

From Eq. (A.2b), it is evident that the stretch which characterizes a certain configuration can be expressed as:

$$\lambda(X) = \left(\frac{R_0}{r(X)}\right)^2. \tag{A.3}$$

To distinguish in this "total" stretch a contribution from uniform deformation and another one from post-necking deformation, it is possible to introduce the radius $r^*$ at the necking onset as follows:

$$\lambda(X) = \left(\frac{R_0}{r^*}\frac{r^*}{r(X)}\right)^2 = \left(\frac{R_0}{r^*}\right)^2\left(\frac{r^*}{r(X)}\right)^2. \tag{A.4}$$

By comparing Eq. (A.4) with Eq. (A.3), it is possible to observe that the first term represents the stretch at the necking onset (i.e., that at the maximum uniform deformation):

$$\lambda_u = \left(\frac{R_0}{r^*}\right)^2. \tag{A.5}$$

The remaining term of Eq. (A.4) then represents the contribution of the post-necking deformation to the "total" stretch. It will be denoted as $\lambda_p$:

$$\lambda_p(X) = \left(\frac{r^*}{r(X)}\right)^2. \tag{A.6}$$

Therefore, Eq. (A.4) can be written as:

$$\lambda(X) = \lambda_u\lambda_p(X). \tag{A.7}$$

Consider now two cylinders made of two materials, 1 and 2, and characterized by the same necking shape (in relative terms). It means that the pairs $\left(x_1/r_1^*, r_1/r_1^*\right)$ overlap with the pairs $\left(x_2/r_2^*, r_2/r_2^*\right)$. Equivalently, the pairs $(x_1, r_1)$ and $(kx_2, kr_2)$ are overlapped, being $k = r_1^*/r_2^*$. However, it is not straightforward to understand which are the material points that are equivalent in the two materials. In other words, which $j$-th point of material 2 is equivalent to the $i$ th point of material 1, i.e., which are $i$ and $j$ so that:

$$x_{1i} = kx_{2j}; \tag{A.8a}$$

$$r_{1i} = kr_{2j}. \tag{A.8b}$$

Consider now that the points are identified by their position in the initial configuration $(X_{1i}, R_{1i})$ and $\left(X_{2j}, R_{2j}\right)$. Since the points under analysis are on the specimen surface and that the specimens have the same initial geometry, the initial radial coordinates are the same: $R_{1i} = R_{2j} = R_0$. Hence, they can be simply identified by their initial axial coordinates $X_{1i}$ and $X_{2j}$.

With the aim of finding the relationship between $X_{1i}$ and $X_{2j}$, i.e., the initial axial positions of material points that are analogous for the post-necking phase, Eq. (A.8a) is imposed and each term is expressed through Eq. (A.2a):

$$x_{1i} = \Lambda_{1i} + \frac{1}{4\,\lambda_{1i}^3}\left.\frac{d\lambda_1}{dX_1}\right|_{X_{1i}}\frac{R_0^2}{2}; \tag{A.9a}$$

$$x_{2j} = \Lambda_{2j} + \frac{1}{4\,\lambda_{2j}^3}\left.\frac{d\lambda_2}{dX_2}\right|_{X_{2j}}\frac{R_0^2}{2}. \tag{A.9b}$$

Focusing on the first addendum, the following expressions can be found:

$$\Lambda_{1i} = \int_0^{X_{1i}}\lambda_1(X_1)dX_1 = \int_0^{X_{1i}}\lambda_{u1}\lambda_{p1}(X_1)dX_1 = \lambda_{u1}\int_0^{X_{1i}}\lambda_{p1}(X_1)dX_1 \tag{A.10a}$$

and similarly:

$$\Lambda_{2j} = \lambda_{u2}\int_0^{X_{2j}}\lambda_{p2}(X_2)dX_2. \tag{A.10b}$$

Considering that Eqs. (A.6) and (A.8b) together prove that the post-necking stretch is the same, i.e.:

$$\lambda_{p1}(X_{1i}) = \lambda_{p2}(X_{2j}) \tag{A.11}$$

or more concisely $\lambda_{p1i} = \lambda_{p2j}$, then it is possible to make a change of variables in Eq. (A.10) (by reasonably assuming that $\frac{dX_1}{dX_2} = c$):

$$\Lambda_{1i} = \lambda_{u1}\int_0^{X_{2j}} \lambda_{p2}(X_2)dX_2 c = c\lambda_{u1}\frac{\Lambda_{2j}}{\lambda_{u2}} = \frac{c}{k^2}\Lambda_{2j}. \tag{A.12}$$

In the last step, it has been considered that:

$$\frac{\lambda_{u1}}{\lambda_{u2}} = \frac{\left(R_0/r_1^*\right)^2}{\left(R_0/r_2^*\right)^2} = \left(\frac{r_2^*}{r_1^*}\right)^2 = \frac{1}{k^2}. \tag{A.13}$$

Focusing, then, on the stretch derivative of Eqs. (A.9), the following expressions hold (using first Eq. (A.7) and then Eq. (A.6)):

$$\left.\frac{d\lambda_1}{dX_1}\right|_{X_{1i}} = \lambda_{u1}\left.\frac{d\lambda_{p1}}{dX_1}\right|_{X_{1i}} = \lambda_{u1}\frac{d}{dX_1}\left(\frac{r_1^*}{r_1(X_1)}\right)^2 = \lambda_{u1}r_1^{*2}\left(-2\frac{dr_1}{dX_1}\frac{1}{r_1^3(X_1)}\right) = -\lambda_{u1}\frac{2r_1^{*2}}{r_1^3(X_1)}\frac{dr_1}{dX_1} \tag{A.14a}$$

and similarly:

$$\left.\frac{d\lambda_2}{dX_2}\right|_{X_{2j}} = -\lambda_{u2}\frac{2r_2^{*2}}{r_2^3(X_2)}\frac{dr_2}{dX_2}. \tag{A.14b}$$

Then, in Eq. (A.14a) $r_1(X_1)$ is replaced with $kr_2(X_2)$ for Eq. (A.8b):

$$\left.\frac{d\lambda_1}{dX_1}\right|_{X_{1i}} = -\frac{\lambda_{u2}}{k^2}\frac{2r_1^{*2}}{k^3r_2^3(X_2)}k\frac{dr_2}{dX_2}\frac{dX_2}{dX_1} = -\frac{\lambda_{u2}}{k^2}\frac{2r_1^{*2}}{k^2r_2^3(X_2)}\frac{dr_2}{dX_2}\frac{1}{c}. \tag{A.15}$$

From Eq. (A.14b), it results that:

$$\lambda_{u2}\frac{2}{r_2^3(X_2)}\frac{dr_2}{dX_2} = -\frac{1}{r_2^{*2}}\left.\frac{d\lambda_2}{dX_2}\right|_{X_{2j}}. \tag{A.16}$$

So, Eq. (A.15) becomes:

$$\left.\frac{d\lambda_1}{dX_1}\right|_{X_{1i}} = \frac{1}{k^4}\frac{r_1^{*2}}{r_2^{*2}}\frac{1}{c}\left.\frac{d\lambda_2}{dX_2}\right|_{X_{2j}} = \frac{1}{k^2c}\left.\frac{d\lambda_2}{dX_2}\right|_{X_{2j}}. \tag{A.17}$$

Therefore, plugging Eqs. (A.12) and (A.17) into Eq. A.9a, the result is:

$$x_{1i} = \frac{c}{k^2}\Lambda_{2j} + \frac{k^6}{4}\frac{1}{\lambda_{2j}^3}\frac{1}{k^2c}\left.\frac{d\lambda_2}{dX_2}\right|_{X_{2j}}\frac{R_0^2}{2}. \tag{A.18}$$

Finally, to get $x_{1i} = kx_{2j}$ (Eq. (A.8a)), $c$ must be equal to $k^3$.
Hence, the initial axial positions of material points that are analogous for the post-necking phase are linked through the relationship: $X_{1i} = k^3X_{2j}$.

## Appendix B

Consider a strain-dependent TQC, the integral TQC represents the integral average of the differential TQC:

$$\beta_{int}(\varepsilon) = \frac{1}{\varepsilon}\int_0^{\varepsilon}\beta_{diff}(\tilde{\varepsilon})\,d\tilde{\varepsilon}. \tag{B.1}$$

To derive the inverse formula, let's define $B(\varepsilon)$ as the indefinite integral of $\beta_{diff}$:

$$B(\varepsilon) = \int \beta_{diff}(\varepsilon)d\varepsilon. \tag{B.2}$$

Then, by plugging Eq. (B.2) into Eq. (B.1), it results that:

$$\beta_{int} = \frac{1}{\varepsilon}(B(\varepsilon) - B(0)) \tag{B.3}$$

and hence:

$$B(\varepsilon) = \beta_{int}\varepsilon + B(0). \tag{B.4}$$

Since it holds from Eq. (B.2) that:

$$\beta_{diff} = \frac{dB}{d\varepsilon}, \tag{B.5}$$

Eq. (B.4) can be used to finally obtain that:

$$\beta_{diff}(\varepsilon) = \frac{d\beta_{int}}{d\varepsilon}\varepsilon + \beta_{int}. \tag{B.6}$$

This allows one to analytically derive $\beta_{diff}(\varepsilon)$ knowing $\beta_{int}(\varepsilon)$ which can be obtained experimentally in a more stable way than $\beta_{diff}(\varepsilon)$.

## Data availability

Data will be made available on request.

## References


[1] Nassar O. On the conversion of plastic work into heat in metals. In: Proceedings A. 481. The Royal Society; 2025, 20240139.
[2] Taylor GI, Quinney H. The latent energy remaining in a metal after cold working. In: Proceedings of the royal society of London. Series A, containing papers of a mathematical and physical character. 143; 1934. p. 307–26.
[3] Mason JJ, Rosakis AJ, Ravichandran G. On the strain and strain rate dependence of the fraction of plastic work converted to heat: an experimental study using high speed infrared detectors and the Kolsky bar. Mech Mater 1994;17(2–3):135–45.
[4] Bever MB, Holt DL, Titchener AL. The stored energy of cold work. Prog Mater Sci 1973;17:5–177.
[5] Hodowany J, Ravichandran G, Rosakis AJ, Rosakis P. Partition of plastic work into heat and stored energy in metals. Exp Mech 2000;40:113–23.
[6] Macdougall D. Determination of the plastic work converted to heat using radiometry. Exp Mech 2000;40:298–306.
[7] Rittel D, Zhang LH, Osovski S. The dependence of the Taylor–Quinney coefficient on the dynamic loading mode. J Mech Phys Solids 2017;107:96–114.
[8] Zhang T, Guo ZR, Yuan FP, Zhang HS. Investigation on the plastic work-heat conversion coefficient of 7075-T651 aluminum alloy during an impact process based on infrared temperature measurement technology. Acta Mech Sin 2018;34:327–33.
[9] Vazquez-Fernandez NI, Soares GC, Smith JL, Seidt JD, Isakov M, Gilat A, Hokka M. Adiabatic heating of austenitic stainless steels at different strain rates. J Dyn Behav Mater 2019;5:221–9.
[10] Soares GC, Hokka M. The Taylor–Quinney coefficients and strain hardening of commercially pure titanium, iron, copper, and tin in high rate compression. Int J Impact Eng 2021;156:103940.
[11] Kingstedt O, Lew A, Pratt M, Salehi SD, Rao S. Investigation of thermomechanical coupling in Inconel 718 at homologous temperatures of 0.2 and 0.5. Metall Mater Trans A 2024;55(9):3591–600.
[12] Lew A, Loeffler C, Varga J, Jones A, Salehi SD, Kingstedt OT. A comparison of techniques to measure the conversion of plastic work to heat in 304L stainless steel under adiabatic conditions. Int J Impact Eng 2025;198:105220.
[13] Smith JL, Seidt JD, Fietek CJ, Gilat A. Taylor-Quinney coefficient determination from simultaneous strain and temperature measurements of uniform and localized deformation in tensile tests. J Mech Phys Solids 2025;199:106099.
[14] Aravas N, Kim KS, Leckie FA. On the calculations of the stored energy of cold work. J Eng Mater Technol 1990;112:465–70.
[15] Zehnder AT. A model for the heating due to plastic work. Mech Res Commun 1991;18(1):23–8.
[16] Rosakis P, Rosakis AJ, Ravichandran G, Hodowany J. A thermodynamic internal variable model for the partition of plastic work into heat and stored energy in metals. J Mech Phys Solids 2000;48(3):581–607.
[17] Lieou CK, Bronkhorst CA. Thermomechanical conversion in metals: dislocation plasticity model evaluation of the Taylor-Quinney coefficient. Acta Mater 2021;202:170–80.
[18] Kingstedt OT, Lloyd JT. On the conversion of plastic work to heat in Mg alloy AZ31B for dislocation slip and twinning deformation. Mech Mater 2019;134:176–84.
[19] Benzerga AA, Bréchet Y, Needleman A, Van der Giessen E. The stored energy of cold work: predictions from discrete dislocation plasticity. Acta Mater 2005;53(18):4765–79.
[20] Kositski R, Mordehai D. Employing molecular dynamics to shed light on the microstructural origins of the Taylor-Quinney coefficient. Acta Mater 2021;205:116511.
[21] Rittel D. On the conversion of plastic work to heat during high strain rate deformation of glassy polymers. Mech Mater 1999;31(2):131–9.
[22] Kapoor R, Nemat-Nasser S. Determination of temperature rise during high strain rate deformation. Mech Mater 1998;27(1):1–12.
[23] Goviazin GG, Shirizly A, Rittel D. A comparative study of the performance of IR detectors vs. high-speed cameras under dynamic loading conditions. Exp Mech 2023;63(1):115–24.
[24] Chrysochoos A, Louche H. An infrared image processing to analyse the calorific effects accompanying strain localisation. Int J Eng Sci 2000;38(16):1759–88.
[25] Louche H, Chrysochoos A. Thermal and dissipative effects accompanying Lüders band propagation. Mater Sci Eng: A 2001;307(1–2):15–22.
[26] Schlosser P, Louche H, Favier D, Orgéas L. Image processing to estimate the heat sources related to phase transformations during tensile tests of NiTi tubes. Strain 2007;43(3):260–71.
[27] Dumoulin S, Louche H, Hopperstad OS, Børvik T. Heat sources, energy storage and dissipation in high-strength steels: experiments and modelling. Eur J Mech-A/Solids 2010;29(3):461–74.
[28] Louche H, Vacher P, Arrieux R. Thermal observations associated with the Portevin–Le Châtelier effect in an Al–Mg alloy. Mater Sci Eng: A 2005;404(1–2):188–96.
[29] Ait-Amokhtar H, Fressengeas C, Boudrahem S. The dynamics of Portevin–Le Chatelier bands in an Al–Mg alloy from infrared thermography. Mater Sci Eng: A 2008;488(1–2):540–6.
[30] Soares GC, Vázquez-Fernández NI, Hokka M. Simultaneous full-field strain and temperature measurements in high strain rate testing. Advances in experimental impact mechanics. Elsevier; 2022. p. 255–85.
[31] Pottier T, Toussaint F, Louche H, Vacher P. Inelastic heat fraction estimation from two successive mechanical and thermal analyses and full-field measurements. Eur J Mech-A/Solids 2013;38:1–11.
[32] Knysh P, Korkolis YP. Determination of the fraction of plastic work converted into heat in metals. Mech Mater 2015;86:71–80.
[33] Nowak M, Maj M. Determination of coupled mechanical and thermal fields using 2D digital image correlation and infrared thermography: numerical procedures and results. Arch Civ Mech Eng 2018;18:630–44.
[34] Dæhli LEB, Johnsen J, Berstad T, Børvik T, Hopperstad OS. An experimental–numerical study on the evolution of the Taylor–Quinney coefficient with plastic deformation in metals. Mech Mater 2023;179:104605.
[35] Gilat A, Kuokkala VT, Seidt JD, Smith JL. Full-field measurement of strain and temperature in quasi-static and dynamic tensile tests on stainless steel 316L. Procedia Eng 2017;207:1994–9.
[36] Seidt JD, Kuokkala VT, Smith JL, Gilat A. Synchronous full-field strain and temperature measurement in tensile tests at low, intermediate and high strain rates. Exp Mech 2017;57:219–29.
[37] Smith JL, Seidt JD, Gilat A. Full-field determination of the Taylor-Quinney coefficient in tension tests of Ti-6Al-4V at strain rates up to 7000s-1. In: Proceedings of the 2018 annual conference on experimental and applied mechanics. 3. Springer International Publishing; 2019. p. 133–9.
[38] Beltramo M, Peroni L, Scapin M. A data-driven procedure for the analysis of high strain rate tensile tests via visible and infrared image processing. Int J Impact Eng 2025:105232.
[39] Rittel D, Ravichandran G, Venkert A. The mechanical response of pure iron at high strain rates under dominant shear. Mater Sci Eng: A 2006;432(1–2):191–201.
[40] Audoly B, Hutchinson JW. Analysis of necking based on a one-dimensional model. J Mech Phys Solids 2016;97:68–91.
[41] Audoly B, Hutchinson JW. One-dimensional modeling of necking in rate-dependent materials. J Mech Phys Solids 2019;123:149–71.
[42] Beltramo M, Scapin M, Peroni L. An advanced post-necking analysis methodology for elasto-plastic material models identification. Mater Des 2023;230:111937.
[43] Johnson GR. A constitutive model and data for metals subjected to large strains, high strain rates and high temperatures. In: Proceedings of the 7th international symposium on ballistics1983; 1983.
[44] Peroni L, Scapin M, Song B. Dynamic behavior of metals and alloys designed for high-temperature applications. Dynamic behavior of materials. Elsevier; 2024. p. 339–72.
[45] Scapin M, Peroni L, Carra F. Investigation and mechanical modelling of pure molybdenum at high strain-rate and temperature. J Dyn Behav Mater 2016;2:460–75.
[46] Salehi SD, Kingstedt O. Critical assessment and demonstration of high-emissivity coatings for improved infrared signal quality for Taylor–Quinney coefficient experimentation. Int J Impact Eng 2023;178:104593.
[47] Rittel D, Bhattacharyya A, Poon B, Zhao J, Ravichandran G. Thermomechanical characterization of pure polycrystalline tantalum. Mater Sci Eng: A 2007;447(1–2):65–70.
[48] Zehnder AT, Babinsky E, Palmer T. Hybrid method for determining the fraction of plastic work converted to heat. Exp Mech 1998;38:295–302.